Geometric amplification and suppression of ice-shelf basal melt in West Antarctica

Jan De Rydt[1] and Kaitlin Naughten[2]

[1]Department of Geography and Environmental Sciences, Northumbria University, Newcastle upon Tyne, UK
[2]British Antarctic Survey, Cambridge, UK

Correspondence: Jan De Rydt (jan.rydt@northumbria.ac.uk)

Abstract. Glaciers along the Amundsen Sea coastline in West Antarctica are dynamically adjusting to a change in ice-shelf mass balance that has triggered their retreat and speed-up prior to the satellite era. In recent decades, the ice shelves have continued to thin, albeit at a decelerating rate, whilst ice discharge across the grounding lines has been observed to increase by up to 100% since the early 1990s. Here, the ongoing evolution of ice-shelf mass balance components is assessed in a high-resolution coupled ice-ocean model that includes the Pine Island, Thwaites, Crosson and Dotson ice shelves. For a range of idealized ocean-forcing scenarios, the combined evolution of ice-shelf geometry and basal melt rates is simulated over a 200-year period. For all ice-shelf cavities, a reconfiguration of the 3D ocean circulation in response to changes in cavity geometry is found to cause significant and sustained changes in basal melt rate, ranging from a 75% decrease up to a 75% increase near the grounding lines, irrespective of the far-field forcing. These previously unexplored feedbacks between changes in ice-shelf geometry, ocean circulation and basal melting have a demonstrable impact on the net ice-shelf mass balance, including grounding line discharge, at multidecadal timescales. They should be considered in future projections of Antarctic mass loss, alongside changes in ice-shelf melt due to anthropogenic trends in the ocean temperature and salinity.

1 Introduction

Widespread ~~dynamic~~ thinning of glaciers along the Amundsen coastline in West Antarctica has contributed about 2000 giga-tonnes of ice, or about 5.5 mm, to global mean sea level rise between 1979 and 2017 (Rignot et al., 2019; Shepherd et al., 2019). The region includes the Pine Island, Thwaites, Pope and Smith glaciers (Fig. 1), which currently account for approximately 45% of excess ice discharge from the Antarctic Ice Sheet. The timing and underlying cause for the concurrent and spatially coherent ~~imbalance~~ mass loss of these glacier basins remains a subject of ongoing research (Holland et al., 2022). However, it is understood that a critical role in the present-day evolution of the region's mass balance is played by ocean-induced ablation of its floating ice shelves (Pritchard et al., 2012; Gudmundsson et al., 2019; Smith et al., 2020). ~~In~~ For future decades to centuries, numerical mass balance projections indicate that the Amundsen basin is likely to remain Antarctica's dominant contributor to

sea level rise (Seroussi et al., 2020; Edwards et al., 2021)~~,~~. This persists despite significant uncertainties in climate forcing and poorly represented physical processes, such as ice-shelf melting and temporal changes in ice rheology, basal sliding and ice front location.

A known role in the future evolution of the Ice Sheet's mass balance is played by the evolving buttressing capacity of the ice shelves. Any differences in back pressure due to changes in the structural integrity or geometry of the ice shelves ~~,~~ affect the force balance at the grounding line, and have the potential to impact on the dynamics of the upstream grounded ice (see e.g. Haseloff and Sergienko (2018) and Pegler (2018)). For this reason, changes in the mass balance of the ice shelves play a crucial role in moderating future mass loss from the Antarctic Ice Sheet. At present, ice shelves in the Amundsen Embayment have a negative net mass balance (Adusumilli et al., 2018) as losses from basal ablation and ice-front calving outweigh the input of mass through grounding line fluxes and, to a much smaller extent, surface accumulation. This imbalance is the direct cause for the dynamic response of the adjacent glaciers (Gudmundsson et al., 2019).

Whilst the link between contemporary ice-shelf thinning and increased grounding line flux of Pine Island, Thwaites and other glaciers in the region has been well established, the future mass balance of the ice shelves and related impacts on grounding line discharge remain uncertain. In recent decades, ice-shelf thinning rates in the Amundsen Sea have decreased (Adusumilli et al., 2018)~~due to~~, despite an up to two-fold increase in grounding line flux (Mouginot et al., 2014; Davison et al., 2023; Otosaka et al., 2023)~~and in the absence of a demonstrable positive anomaly in the region's ocean heat content that could sustain anomalously high melt rates (Jenkins, 2016). A~~. A combination of processes that could have led to a reduction in basal melting, such as shoaling of the ice-shelf base and potential deepening of the thermocline depth on the continental shelf, has been suggested as a potential cause (Paolo et al., 2023). However, validating the delicate interplay between different ice-shelf mass balance components in the absence of a long-term and reliable record of ice surface velocities, ice-atmosphere interactions and ocean hydrography remains a difficult problem. Hypothetically, a continued decrease in ice-shelf thinning could drive the system towards a new steady state, although there is no evidence from numerical simulations that such a steady state can be obtained under present-day ocean and atmospheric conditions ~~(Arthern and Williams, 2017; Reese et al., 2023, e.g.)~~ (Arthern and Williams, 2017; Reese et al., 2023).

The rate at which glaciers in the Amundsen basin will continue to lose mass over the next decades to centuries ~~,~~ is controlled by several interrelated mechanisms. Firstly, changes in ice front location, loss of pinning points and ice damage evolution have all been shown to strongly impact on ice-shelf buttressing and grounding line discharge (Lhermitte et al., 2020; Joughin et al., 2019, 2021; De Rydt et al., 2021). Secondly, climatic trends in ocean and atmospheric forcing can lead to a sustained shift in ice-shelf basal and/or surface ablation, and promote long-term changes in ice-shelf mass balance (Jourdain et al., 2022b). A third, as-of-yet poorly understood process, is the potential feedback between changes in the geometry of ice-shelf cavities ~~,~~ and the ocean dynamics that determines the melt rates for a given far-field distribution of temperature and salinity. Whilst ~~such~~ melt-geometry feedbacks have been suggested to play a role in the recent decrease in thinning of the Amundsen Sea ice shelves (Paolo et al., 2023) and they have been studied for idealized geometries (De Rydt and Gudmundsson, 2016, e.g.) and the Thwaites Ice Shelf (Holland et al., 2023), little is known about their possible long-term impact on the net mass balance of

the West Antarctic ice shelves. Nor has the impact of geometry-driven changes in melt been compared to natural (seasonal to decadal) variability or projected anthropogenic trends in far-field ocean conditions.

From an ocean modelling point of view, the past evolution of basal melt rates in the Amundsen Sea (Naughten et al., 2022) and future projections under varying climate change scenarios (Jourdain et al., 2022a)(Jourdain et al., 2022a; Naughten et al., 2023) , have been assessed for fixed, present-day cavity geometries. For the fast retreating glaciers in the Amundsen Sea, this assumption represents an important limitation of current basal mass balance projections. In ice-sheet models, on the other hand, melt rates and their dependency on ice-shelf geometry are commonly simulated using simplified parameterizations that do not retain knowledge about the complex, evolving 3D distribution of heat and salt within the ice shelf cavities. State-of-the-art projections of future mass loss from the Antarctic Ice Sheet, as presented by (Edwards et al., 2021, e.g.)Edwards et al. (2021), therefore lack the physical basis to accurately represent the coupling between changes in cavity geometry and ice-shelf basal ablation.

The current work presents a step towards bridging the gap between both incomplete modelling approaches, and assesses the importance of mutual feedbacks between ocean-driven melt rates and changes in cavity geometry. Starting from a numerical representation of the present-day state of the Amundsen Embayment and adjacent Ice Sheet (Fig. 1), a series of 200-yr long simulations of the Pine Island, Thwaites, Crosson and Dotson glaciers and ice shelves is presented. All simulations were conducted using a newly developed configuration of the coupled ice sheet-ocean model Úa-MITgcm (Naughten and De Rydt, 2023), with a mutually evolving dynamical ice sheet and 3D ocean. Significant changes in the geometry of all ice-shelf cavities were simulated over the 200-yr period for a range of forcing scenarios, and a detailed analysis of the impact on the 3D cavity circulation and basal melt rates is presented. Geometrically-driven changes in melt are compared to changes caused by natural decadal variability in ocean conditions on the Amundsen continental shelf, and the significance of melt-geometry feedbacks for the overall mass balance of the ice shelves, including grounding line fluxes, is assessed.

The remainder of this paper is structured as follows. A detailed overview of the coupled ice-ocean model and experimental design is provided in Sect. 2. The necessary technical background for the analysis of ice-shelf basal melt rates in response to changes in cavity geometry is introduced in Sect. 3. This includes the definition of the 'cavity transfer coefficients' that link average melt rates in the vicinity of the grounding line to the thermal driving of the inflow across the ice front. In Sects. 4 and 5 the analysis of three numerical experiments is presented, focused on the ocean processes that drive changes in basal melt in response to evolving ice-shelf cavities and the relative importance of decadal variations in far-field ocean conditions. A glaciological perspective and the importance of melt-geometry feedbacks for the net mass balance of the ice shelves, including grounding line discharge, is presented in Sect. 6, followed by conclusions and future perspectives in Sect. 7.

2 Numerical setup and experiments

Basal ablation of ice shelves in the Amundsen Sea locally exceeds $100\,\mathrm{m\,yr^{-1}}$ due to the presence of modified Circumpolar Deep Water (mCDW) with temperatures several degrees above the local freezing point (Jacobs and Hellmer, 1996). Whilst mCDW is continuously present on the continental shelf (see Fig. 1), mean melt rates are strongly modulated by decadal variations in the thickness of the mCDW layer (Dutrieux et al., 2014). However, direct observations of ocean variability on the
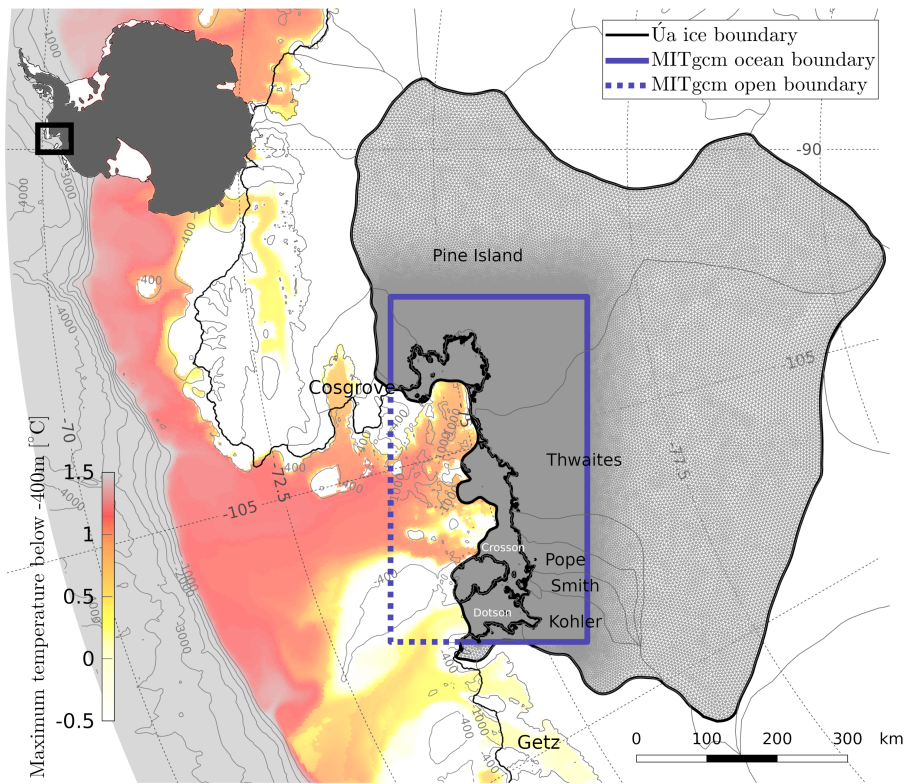
Figure 1. Study area, showing its location in West Antarctica (inset in the top left) and boundaries of the Úa (ice) and MITgcm (ocean) model domains. The Úa domain includes the Pine Island, Thwaites, Crosson and Dotson ice shelves, delineated in black, and drainage basins of their tributary glaciers (Rignot et al., 2019), shown in light grey. The dashed blue line corresponds to the open boundary of MITgcm, where ocean restoring conditions are imposed, as described in Sect. 2.1. The background colour scale corresponds to a 1994-2013 climatology of maximum ocean temperatures below 400 m, averaged over the ensemble of PACE simulations from Naughten et al. (2022). Bathymetric contour lines for the open ocean are from (Morlighem et al., 2020).

90   continental shelf remain sparse, and knowledge about the distribution of heat and salt within the ice-shelf cavities largely relies on the use of general circulation models.

     The ocean currents that cross the ice front and transport thermal energy towards the ice-ocean interface ~~,~~ are steered by the topography of the seafloor and ice-shelf base. Away from sources of barotropic potential vorticity, the depth-averaged flow is approximately aligned with contours of constant water column thickness ~~(Patmore et al., 2019, e.g.)~~ (Patmore et al., 2019)

95 and as a result, sharp gradients in topography such as the ice front (Bradley et al., 2022) or bathymetric sills (De Rydt and Gudmundsson, 2016; Zhao et al., 2019), can impose significant barriers to the flow. The baroclinic transport, on the other hand, is primarily driven by melt-induced stratification, which is affected by geometrical factors such as the gradient of the ice-shelf base.

To simulate the 3D structure of ocean currents in the geometrically complex cavities of the Amundsen Sea, the MIT general
circulation model (MITgcm) with thermodynamically active ice shelves (Marshall et al., 1997; Losch, 2008) was used. To
capture the 2-way feedbacks between changes in ice-shelf geometry and basal melt whilst the ice sheet evolves over time,
MITgcm was coupled to the ice flow model Úa (Gudmundsson et al., 2012; Gudmundsson, 2020), as described in detail below.
The coupled ice-ocean model, Úa-MITgcm, was first developed for simulations of an idealized, Pine Island-like setup by
De Rydt and Gudmundsson (2016), and subsequently adapted by Naughten et al. (2021) (see their methods section for details).
The model setup is described in more detail in Sect. 2.1, followed by an overview of the experimental design in Sect. 2.2.

2.1 Coupled ice-ocean model setup

The MITgcm domain covers a 138,000 km^2 region of the Amundsen continental shelf between 97°W and 116°W, and 73°S and
77°S, delineated by the blue box in Figure 1. The domain includes the present-day Pine Island, Thwaites, Crosson and Dotsen
ice shelf cavities with a buffer of grounded ice to allow upstream migration of the grounding line. The northern and western
edges of the domain were chosen to fully cover the present-day extent of the aforementioned ice shelves and their respective
mCDW inflow pathways but exclude the adjacent Cosgrove Ice Shelf in the east and Getz Ice Shelf in the west. MITgcm
solves the Boussinesq and hydrostatic form of the Navier Stokes equations on an Arakawa C grid in polar stereographic
coordinates with a uniform Eddy-permitting horizontal resolution of 1.3 km. The z-coordinate levels consist of 80 layers with
20 m resolution down to a depth of ~~1600~~ -1600 m, and 10 ~~vertical levels~~ layers with 40 m resolution down to ~~2000~~ -2000 m.
Although the seafloor in the ocean domain is above -1600 m in most places and no deeper than -1730 m at present, vertical
layers down to -2000 m were added to accommodate future retreat of the grounding lines into deeper terrain. The deep basins
of Kohler and Thwaites glaciers in particular, reach depths down to -2000m. The horizontal and vertical grid resolution were
optimized to comply with the extent of the ocean domain, the parallel software architecture of MITgcm and the available
computational resources on the UK HPC facility ARCHER2 (www.archer2.ac.uk). MITgcm uses partially filled cells with a
minimum thickness of 1 m to allow greater flexibility of the piecewise ~~linear~~ constant representation of the bathymetry and
ice-shelf draft. At the northern and western open boundaries of the domain (dashed blue line in Figure 1), restoring conditions
for temperature, salinity and velocities were applied across a 6.5 km wide sponge layer, with restoring timescales ranging from
3 hrs at the boundary to 6 hrs in the interior. Further details about the boundary conditions are provided in Sect. 2.2.

In all experiments ocean surface fluxes (heat, salt, momentum) were ignored, and variability in water mass properties was
imposed solely through restoring at the northern and western open boundaries. The absence of surface fluxes prevents a realistic
representation of the ocean mixed layer and eliminates polynya activity that can cause deep convection. However, for the
purpose of this study, such processes are thought to be of secondary importance. Rather than analyze the connection between
offshore atmospheric conditions, variability in water mass properties and basal melt, the focus will be on the links between
changes in cavity geometry and basal melt for given far-field ocean conditions. ~~Moreover, the forthcoming analysis will be~~
~~primarily restricted to the analysis of thermohaline properties in the deepest parts of the cavities, which are thought to be~~
~~largely unaffected by changes in surface waters.~~

~~Ice-shelf~~ In line with previous studies (e.g. Goldberg et al. (2019) and Naughten et al. (2022)), ice-shelf melt rates in MIT-gcm were computed using the 3-equation formulation for conservation of heat, salt and momentum (Holland and Jenkins, 1999) with ambient temperature and salinity averaged across a 20 m layer below the ice shelf (Losch, 2008) and a linear dependency of the exchange coefficients on the friction velocity averaged over the same layer.

The Úa domain includes the Pine Island, Thwaites, Dotson and Crosson ice shelves and their respective drainage basins (Rignot et al., 2019), as shown by the black outline in Figure 1. The ice front was traced from a Landsat 5 image from 1997 and kept fixed in all simulations. Úa uses finite element methods to solve the vertically integrated shallow shelf (SSA or SSTREAM) equations of ice flow on an unstructured grid with linear triangles. The mean nodal spacing of the mesh is 1.5 km, with local refinement down to 400 m in areas with high strain rates and strain rate gradients. In line with published recommendations to minimize resolution-dependency of the grounding line dynamics (see e.g. Pattyn et al. (2012) and Cornford et al. (2016)), adaptive mesh refinement down to 400 m was used within a 2 km buffer around the moving grounding line. In order to minimize the need for interpolation between the MITgcm and Úa meshes, MITgcm nodes were included as a subset of the Úa nodes at all times. The ice rheology was described using Glen's law with exponent $n = 3$, and basal sliding was parametrized ~~using a~~ by the commonly used non-linear Weertman law with exponent $m = 3$. Ice viscosity and basal slipperiness, which are unknown fields in the rheology and sliding parameterizations, were estimated using an inverse method, as described in App. A. Non-zero melt rates were only applied to nodes of fully floating elements, following the conservative "no-melt parameterization" scheme in Seroussi and Morlighem (2018). A zero flow condition was imposed for the ice divide at the boundary of the mesh.

The Úa-MITgcm coupler (Naughten and De Rydt, 2023) controls the offline exchange of basal melt rates and ice-shelf geometry between the otherwise independent models. The coupling timestep, or frequency at which data is exchanged between models, was set to 30 days. The short coupling interval was favoured to avoid the development of regularly spaced undulations in the ice draft of the Pine Island Ice Shelf, with kilometer-scale wavelength and amplitudes over 100 m. The undulations are not a numerically robust feature of the coupled model, and a coupling timestep was chosen that suppresses their existence. At each coupling timestep, MITgcm melt rates averaged over the coupling period were linearly interpolated onto the Úa grid, and the new Úa ice draft was transferred to MITgcm. Both models were restarted from their final state at the end of the previous coupling timestep. The temperature and salinity of newly opened ocean cells were horizontally extrapolated from neighbouring cells, and velocities of the corresponding water column were corrected to preserve the barotropic transport and avoid a step-change in the flow divergence. In order to enable overturning in shallow water columns, a minimum of two vertical cells was achieved by (temporarily) lowering the bathymetry in MITgcm for small areas of the domain, in particular near the grounding line. Corrections to the bathymetry were less than the vertical resolution of the MITgcm grid.

A detailed overview of the input data sets, initialization and spin up of MITgcm, Úa and the coupled Úa-MITgcm configuration are provided in Appendix A.

2.2 Experimental design

The numerical experiments were designed with two key objectives in mind. Firstly, to quantify feedbacks between future changes in cavity geometry and basal melt rates, and secondly, to compare geometrically-driven changes in melt rate to vari-

ability caused by natural changes in ambient ocean conditions. All experiments were started after the model spin up, with an initial ice-sheet configuration that is close to the present-day state, as detailed in App. A.

In the first set of experiments, cavities were exposed to 200 years of time-invariant far-field ocean conditions, imposed as constant restoring of temperature, salinity and velocities at the open boundaries (Fig. 1). The absence of temporal variability in heat transport at the ocean boundaries allowed all changes in basal melt to be attributed to geometrical feedbacks, hence addressing the first objective outlined above. The restoring conditions were subsampled from an existing hindcast simulation (01/1997-12/2014) of the Amundsen Sea (Kimura et al., 2017), based on a MITgcm configuration with horizontal resolution of 0.1° in longitude and ERA-Interim atmospheric forcing.

The first experiment (see Table 1) corresponds to a 'high melt' scenario, henceforth referred to as *hi_melt*, with monthly average temperature, salinity and velocities from November 2002 imposed as restoring conditions at the open boundaries of the MITgcm domain. The corresponding ocean state has a shallow thermocline and is characteristic for high amplitude, low prevalence conditions within the 1997-2014 frequency distribution of simulated melt rates (see Figures 2 and A3). The choice of November 2002 conditions was solely based on their high melt bias in the histograms in Figure 2. Other selection criteria, such as the net heat flux into the cavities, were considered, but did not lead to a significantly different choice of ocean state or melt rates.

Experiment	Boundary restoring	Ice-shelf geometry	Simulation time
hi_melt	montly average T, S, U, V for 11/2002	evolving	200 yrs
av_melt	monthly average T, S, U, V for 01/1998	evolving	200 yrs
var_melt	time-varying, 11 cycles of 01/1997 - 12/2014	evolving	198 yrs
ref_melt	time-varying, 11 cycles of 01/1997 - 12/2014	fixed present-day	198 yrs

Table 1. Overview of the numerical experiments presented in the main part of the text. All boundary restoring conditions (temperature, salinity, velocities) were obtained from a regional MITgcm configuration of the Amundsen Sea (Kimura et al., 2017).

The second experiment corresponds to an 'average melt' scenario, henceforth referred to as *av_melt*, with average oceanographic conditions from January 1998 imposed at the open boundaries. The corresponding ocean state is characteristic for average amplitude, high prevalence melt rates (Fig. 2), with the exception of the Crosson and Dotson cavities, where conditions are biased towards lower-than-average melt rates. Similar to the *hi_melt* experiment, the choice of January 1998 conditions was based on the histograms in Figure 2, with melt rates that are characteristic for the January 1997-December 2014 period. Other choices of boundary conditions might have led to a comparable ocean state and melt rates but were not tested.

For completeness, a 'low melt' scenario with a deep thermocline was considered, which resulted in a persistently positive mass balance of the ice shelves, and a readvance of the grounding lines. Since this behaviour is unlikely to inform on the future evolution of glaciers in the Amundsen basin, this scenario was not considered further.

In the second set of experiments, time-varying restoring conditions were applied at the MITgcm boundaries. The aim was not to carry out projections for different emissions scenarios, but rather to disentangle geometrical feedbacks from the sensitivity of melt to natural variability in the ocean state. Monthly averaged ocean conditions between January 1997 and December 2014
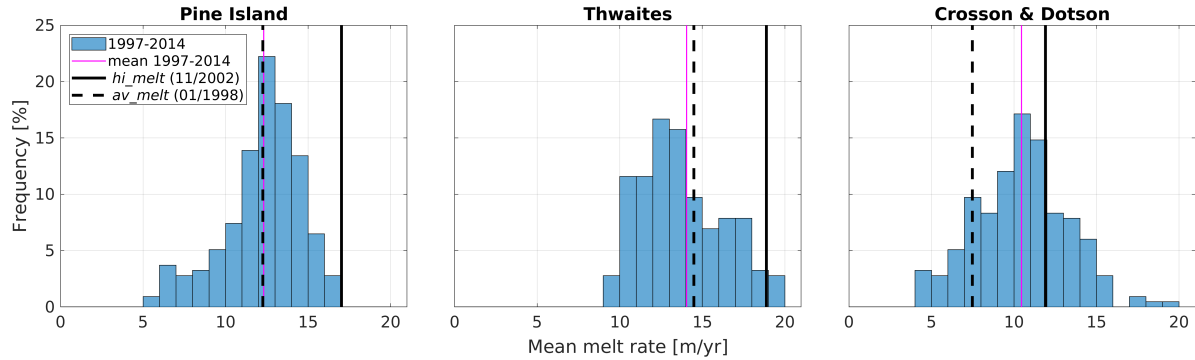
Figure 2. Frequency distribution of monthly mean melt rates for each ice shelf, as simulated during the first cycle of the *var_melt* experiment, covering the January 1997 to December 2014 period. The magenta line indicates the mean melt rate over the entire simulation period. The solid and dashed lines indicate melt rates that correspond to the ocean forcing applied in the *hi_melt* and *av_melt* experiments, respectively.

from (Kimura et al., 2017) were imposed at the MITgcm boundary, and linearly interpolated onto the model time. The 1997-2014 restoring conditions were cyclically repeated 11 times for a total of 198 simulation years. The frequency distribution of melt rates during the first cycle is shown in Figure 2. As well as a coupled ice-ocean simulation with a dynamic ice-shelf geometry (referred to as *var_melt*), a reference stand-alone ocean simulation with fixed ice-shelf cavities was carried out (referred to as *ref_melt*). For both experiments, the variability in basal ablation was analyzed within each 18-year forcing cycle, as well as between successive cycles.

Despite the idealized nature of the ocean forcing, experiments induce an ice-sheet response that is informative for sustained present-day ocean conditions (*av_melt* and *var_melt*) and future climate conditions dominated by warm periods (*hi_melt*). The key advance of this work is the inclusion of ice-ocean feedbacks simulated by a 3D ocean model. As will be argued in Sect. 6, such feedbacks play an important role in the dynamical evolution of the Amundsen Sea glaciers, and results provide a first step towards more definitive climate change scenario-based projections of mass loss in response to ocean-induced ice-shelf thinning over the next decades to centuries.

3   Cavity transfer coefficients

In order to diagnose the feedbacks between changes in basal melt, imposed ocean boundary conditions and cavity geometry, a number of 'cavity transfer coefficients' are introduced. Each time-varying coefficient will be shown to play a distinctive role in linking the far-field ocean properties to the basal melt rates, while their values depend to greater or lesser extent on the complex changes in cavity geometry. More precisely, spatially averaged basal melt rates, denoted by m, can be expressed as a product of the ~~time-varying ocean thermal forcing at the ice front $T_{xIF}(t)$, the 'outer cavity~~ time-dependent 'thermal transfer coefficient' ~~$\mu(t)$, the 'thermal~~ ϵ_T, 'momentum transfer coefficient' ~~$\epsilon_T(t)$, and the 'momentum~~ ϵ_U, 'outer cavity transfer coefficient' ~~$\epsilon_U(t)\mu$,~~

and time-varying ocean thermal driving at the ice front $T_{\star\mathrm{IF}}$, as follows:

$$m(t) = m_0\, \epsilon_T(t)\, \epsilon_U(t)\, \mu(t)^2 \left(T_{\star\mathrm{IF}}(t)\right)^2, \tag{1}$$

where m_0 is a constant defined in Eq. ~~5~~(5). The expression in Eq. ~~1~~(1) can be derived from the fundamental relationships between basal melt and properties of the oceanic mixed layer directly beneath the ice shelf, as follows.

3.1 Basal melt parameterization

Under the assumption that turbulent mixing of heat towards the ice-ocean interface is dominated by shear instabilities in the current, basal melt rates can be parameterized as a function of the thermal driving in the mixed layer, denoted by $T_\star$, and the friction velocity relative to the ice base, denoted by $U_\star$ (Jenkins and Bombosch, 1995):

$$m(\mathbf{x},t) = m_0\, T_\star(\mathbf{x},t)\, U_\star(\mathbf{x},t), \tag{2}$$

with

$$
\begin{aligned}
T_\star(\mathbf{x},t) &= T(\mathbf{x},t) - T_f(\mathbf{x},t), & (3)\\
U_\star(\mathbf{x},t) &= C_d^{1/2} U(\mathbf{x},t), & (4)\\
m_0 &= \frac{\Gamma_T}{(L_i - c_i T_{\star i})/c}, & (5)
\end{aligned}
$$

where ~~$T_f(\mathbf{x},t)$~~ T_f is the salinity-dependent freezing point at the depth of the ice base, and $T_{\star i} = T_f - T_i$ where T_i is the temperature of the ice. Values $C_d = 2.5\times10^{-3}$, $\Gamma_T = 0.02$, ~~$L_i = 3.4\times10^5\,\mathrm{Jkg}^{-1}, c_i = 2.0\times10^3\,\mathrm{Jkg}^{-1\,\circ}\mathrm{C}^{-1}, \text{and } c = 4.0\times10^3\,\mathrm{Jkg}^{-1\,\circ}\mathrm{C}^{-1}$~~ $L_i = 3.4\times10^5\,\mathrm{J\,kg}^{-1}$, $c_i = 2.0\times10^3\,\mathrm{J\,kg}^{-1}\mathrm{K}^{-1}$, and $c = 4.0\times10^3\,\mathrm{J\,kg}^{-1}\mathrm{K}^{-1}$ were used for the quadratic drag coefficient, turbulent heat exchange coefficient, enthalpy of fusion of ice, specific heat capacity of ice and specific heat capacity of water, respectively. In all MITgcm simulations, basal melt rates were calculated using the parameterization in Eq. ~~2, with $T(\mathbf{x},t)$ and $U(\mathbf{x},t)$~~ (2), with T and U calculated as a weighted average of cell properties adjacent to the ice-ocean interface, as described in Sect. 2.1.

3.2 Thermal transfer coefficient ϵ_T

Cells adjacent to the ice-ocean interface will be referred to as the "mixed layer" to indicate that any vertical shear and thermohaline gradients that might exist in a thin boundary layer adjacent to the ice base remain unresolved due to the 20 m vertical resolution of the ocean model. Properties of the mixed layer, and hence basal melt rates, are controlled by the thermal ~~forcing~~ driving of water masses that enter the cavity. In particular, the temperature of the mixed layer is modulated by mixing of the ambient water with meltwater at the local freezing temperature. As a result, the thermal driving of the mixed layer can be defined as a fraction of the average thermal driving of the inflow, $T_{\star\mathrm{in}}$:

$$T_\star(\mathbf{x},t) = \epsilon_T(\mathbf{x},t)\, T_{\star\mathrm{in}}(t), \tag{6}$$

with $0 < \epsilon_T < 1$ a space and time-dependent dimensionless coefficient (Jenkins et al., 2018), which will henceforth be referred to as the 'thermal transfer coefficient'. Details of how $T_{\star\mathrm{in}}$ is calculated are provided in Sect. 3.4.

3.3 Momentum transfer coefficient ϵ_U

Based on inherent properties of the conservation for mass, momentum, heat and salt within the mixed layer, it has been argued that the friction velocity, $U_\star$, also scales approximately linearly with the thermal ~~forcing~~ driving (Holland et al., 2008). Analogous to Eq. ~~6~~ (6), a scaling coefficient, henceforth denoted by ϵ_U and ~~refered~~ referred to as 'momentum transfer coefficient', is introduced to express this relationship:

$$U_\star(\mathbf{x}, t) = \epsilon_U(\mathbf{x}, t) T_{\star\mathrm{in}}(t), \tag{7}$$

where ϵ_U has dimensions ~~m s$^{-1\circ}$C^{-1}~~ m s^{-1}K^{-1}. Combining Eqs. ~~2, 6 and 7~~ (2), (6) and (7) then leads to

$$m(\mathbf{x}, t) = m_0 \, \epsilon_T(\mathbf{x}, t) \, \epsilon_U(\mathbf{x}, t) \left(T_{\star\mathrm{in}}(t) \right)^2, \tag{8}$$

which expresses local melt rates as a quadratic function of the thermal ~~forcing~~ driving, and two transfer coefficients, ϵ_T and ϵ_U, which link the far-field driving to properties of the mixed layer.

3.4 Basal melt in the deep interior cavity

To facilitate the analysis of temporal changes in melt rates, Eq. ~~8~~ (8) can be spatially averaged. One viable choice is to calculate average basal melt rates for each ice shelf, and define $T_{\star\mathrm{in}}$ as the average thermal driving of the inflow across the corresponding ice front. One shortcoming of this simple diagnostic, however, is the loss of information about changes in melt that occur over small areas of glaciological importance, in particular in the vicinity of the grounding line. Since the steepest slopes of ice shelf draft in the Amundsen Sea are typically found near the grounding line, ice-shelf wide averages are dominated by melt rates in the relatively extensive, shallow areas above the thermocline. Since the focus of this study is on geometrical changes and basal melt feedbacks in the deep interior of the cavities, a more appropriate diagnostic will be introduced below.

First, all cavities are divided in an 'outer region' and a 'deep interior', as illustrated for the Pine Island Ice Shelf cavity in Fig. 3. The deep interior is defined as the part of the cavity with ice draft below -400 m. This bound approximates the shallowest depth at which mCDW is currently found on the Amundsen continental shelf (Dutrieux et al., 2014; Jenkins et al., 2018), and the deep interior can be thought of as ice-shelf regions that are directly exposed to (a modified form of) the warmest waters. Secondly, $T_{\star\mathrm{in}}$ is defined as the average thermal driving of the inflow across a vertical section along the -400 m ice draft contour, henceforth denoted by ~~$T_{\star\mathrm{DI}}(t)$~~ $T_{\star\mathrm{DI}}$, where DI refers to Deep Interior. A schematic representation of ~~$T_{\star\mathrm{DI}}(t)$~~ $T_{\star\mathrm{DI}}$ is shown in Figure 3, and calculated as follows:

$$T_{\star\mathrm{DI}}(t) = \frac{1}{L} \int_{b(\mathbf{x})=-400} \frac{1}{H(l)} \left(\int_{B(l)}^{-400} T_\star(l, z, t) \, \theta(U_n) \, \mathrm{d}z \right) \mathrm{d}l, \tag{9}$$

with $L = \int_{b(\mathbf{x})=-400} \mathrm{d}l$ the horizontal length of the section, b and B the ice draft and seafloor depth respectively, $H = b - B$ the water column thickness, $T_\star = T - T_f$ where the freezing temperature T_f is calculated at a given depth z, and θ a Heaviside step function which is zero/one for negative/positive (i.e. outflowing/inflowing) normal velocities U_n. Finally, ~~melt rates are~~
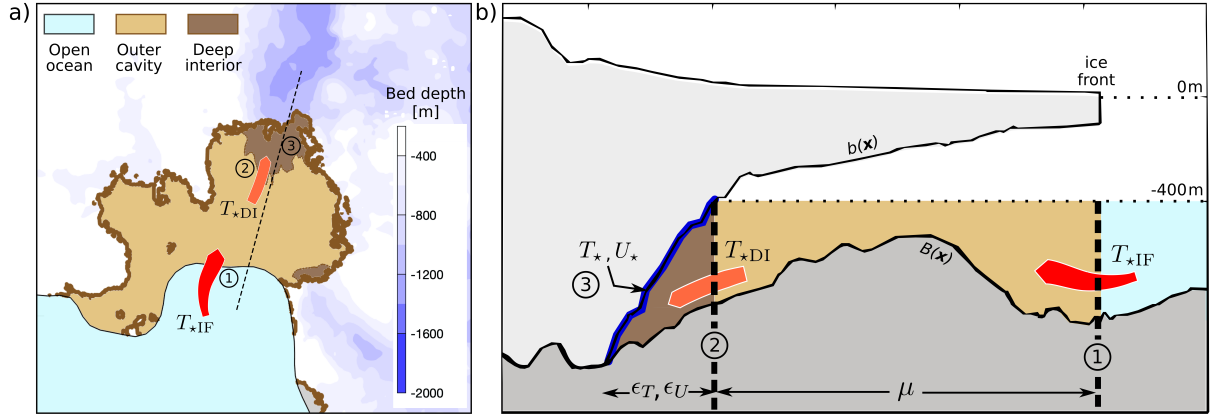
Figure 3. (a) Plan view and (b) section along the dashed line in a) of the Pine Island Ice Shelf, used to illustrate the concepts of the 'outer cavity' and 'deep interior', which correspond to regions of the ice-shelf cavity with draft above and below -400 m, respectively. Key locations referred to in the main text are numbered 1-3: 1) section at the ice front where thermal driving of the inflow below -400 m ($T_{\star\mathrm{IF}}$) is calculated, 2) section at the -400 m ice shelf draft contour where thermal driving of the inflow into the deep cavity is calculated ($T_{\star\mathrm{DI}}$), and 3) the oceanic mixed layer in the deep interior where the thermal deficiency ($\sout{T_\star}T_\star$) and boundary current ($U_\star$) that determine the melt rates are calculated.

~~averaged over~~ the time evolution of average basal melt rates in the deep interior ~~and~~ can be expressed as a function of $T_{\star\mathrm{DI}}$ using Eqs. ~~2, 6 and 7:~~ (2), (6) and (7):

$$\overline{m}_{\mathrm{DI}}(t) := \frac{1}{\mathcal{A}} \int_{b(\mathbf{x}) \leq -400} m(\mathbf{x},t)\ \mathrm{d}\mathbf{x} = \frac{m_0}{\mathcal{A}} \int_{b(\mathbf{x}) \leq -400} T_\star(\mathbf{x},t)\, U_\star(\mathbf{x},t)\ \mathrm{d}\mathbf{x}$$

$$= m_0 \left(\frac{1}{\mathcal{A}} \int_{b(\mathbf{x}) \leq -400} \epsilon_T(\mathbf{x},t)\ \mathrm{d}\mathbf{x} \right) \left(\frac{1}{\mathcal{A}} \int_{b(\mathbf{x}) \leq -400} \epsilon_U(\mathbf{x},t)\ \mathrm{d}\mathbf{x} \right) \left(T_{\star\mathrm{DI}}(t) \right)^2$$

$$+ \operatorname{Cov}\left(T_\star, U_\star \right)$$

$$= m_0\, \overline{\epsilon}_{T,\mathrm{DI}}(t)\, \overline{\epsilon}_{U,\mathrm{DI}}(t) \left(T_{\star\mathrm{DI}}(t) \right)^2 + \operatorname{Cov}\left(T_\star, U_\star \right), \tag{10}$$

In the above derivation, spatial gradients of heat diffusion into the ice were ignored and a constant ~~$T_{\star i} = T_f - T_i = -15°C$~~ $T_{\star i} = T_f - T_i = -15°\mathrm{C}$ was assumed, such that ~~$m_0 \approx 2.2 \times 10^{-4\,°}C^{-1}$~~ $m_0 \approx 2.2 \times 10^{-4}\,\mathrm{K}^{-1}$. Although spatial variations in T_f were accounted for in the calculation of basal melt in MITgcm, corrections are small and will be ignored for the purpose of this analysis. Notations $\overline{\epsilon}_{T,\mathrm{DI}}$ and $\overline{\epsilon}_{U,\mathrm{DI}}$ were introduced to represent coefficients averaged over the deep interior of each ice shelf, and $\mathcal{A}(t) = \int_{b(\mathbf{x}) \leq -400} I\ \mathrm{d}\mathbf{x}$ was used to denote the area of the ice shelf with draft below -400 m. It can be shown that the covariance term $\operatorname{Cov}\left(T_\star, U_\star \right)$ is typically an order of magnitude smaller than the first term on the right hand side, and will be omitted from subsequent analysis.

3.5 Outer cavity transfer coefficient μ

285 Under certain conditions, such as simulations of idealized cavity geometries with a flat bathymetry, properties of the inflow at the ice front propagate into the deep cavity without significant modification. As a result, $T_{\star\mathrm{DI}}$ is approximately equal to the thermal driving of the inflow at the ice front, henceforth denoted by $T_{\star\mathrm{IF}}$ and schematically represented in Figure 3. For realistic cavities with complex geometry and ocean dynamics, however, the ratio between $T_{\star\mathrm{DI}}$ and $T_{\star\mathrm{IF}}$ can be significantly different from one. Indeed, even though the outer cavities in proximity of the ice front are flooded with mCDW, mixing of

290 the mCDW with subglacial meltwater and/or topographic blocking can prevent the inflowing water to reach the deep cavities unmodified. As a result, the ocean properties that drive the onset of subglacial melt plumes in the vicinity of the grounding line are not generally identical to properties of the inflow at the ice front. In order to characterize the relationship between properties of the inflow at the ice front and the thermal driving in the deep interior, the dimensionless, time-dependent 'outer cavity transfer coefficient' $\mu(t)$ μ is introduced:

295 $$T_{\star\mathrm{DI}}(t + \Delta t) = \mu(t)\, T_{\star\mathrm{IF}}(t)\,, \tag{11}$$

where $T_{\star\mathrm{IF}}$ is calculated as follows:

$$T_{\star\mathrm{IF}}(t) = \frac{1}{L} \int\limits_{\mathrm{ice\,front}} \frac{1}{H(l)} \left(\int\limits_{B(l)}^{-400} T_{\star}(l,z,t)\, \theta(U_n)\, \mathrm{d}z \right)\, \mathrm{d}l\,, \tag{12}$$

width $L = \int_{\mathrm{ice\,front}} \mathrm{d}l$ and $H(l) = -B(l) - 400$. The coefficient μ provides an aggregated measure for the impact of outer-cavity ocean processes, including mixing and topographic steering, on the water properties that feed the buoyant melt water

300 plumes. The offset Δt in Eq. 11 (11) accounts for the time lag between water flowing into the cavity at the ice front and reaching the deep interior, which is a measure of the cavity residence time. For a horizontal length scale of 100 km, which is characteristic for the Amundsen Sea ice shelves, and an average barotropic circulation at the ice front between $0.01\,\mathrm{m\,s^{-1}}$ and $0.015\,\mathrm{m\,s^{-1}}$, the residence time is on the order of a few months. Since the far-field ocean conditions vary predominantly at interannual to decadal timescales, changes in the inflow evolve slowly compared to the cavity residence time, and Δt can be

305 set to zero to good approximation.

Only currents below -400 m are considered in the calculation of $T_{\star\mathrm{IF}}$, for several reasons. Firstly, water masses that access the cavity at depth form the most important source of basal meltwater production in the deep interior. Secondly, the cavity inflow above -400 m predominantly alters the mixed layer properties and melt rates in the outer cavity. Although changes in the ice-shelf draft at the ice front caused significant variations in the shallow currents in some of the Úa-MITgcm simulations,

310 they have little impact on the melt rates in the deep interior, and will not be analysed here. Finally, as pointed out in Sect. 2, the model does not simulate surface processes in the open ocean, such as wind stress, or heat and salt fluxes. Properties of the upper water column and deeper waters in areas with convective mixing are therefore not reliably represented. Several sensitivity tests (not shown here) indicate that results presented in subsequent sections are not critically dependent on the choice of the cut-off depth, and no notable differences were found if either -300 m or -500 m was used to define $T_{\star\mathrm{IF}}$ instead.

315 In summary, Eq. 10 and

3.6 Summary and application to MITgcm

~~Eq. 11~~Equations (10) and (11) can be combined to express the average melt of the deep interior cavity as a function of the ~~far-field thermal forcing, the~~ thermal and momentum transfer coefficients ϵ_T and ϵ_U, ~~and~~ the outer cavity transfer coefficient μ, and the average thermal driving of the inflow at the ice front $T_{\star\text{IF}}$, as expressed in Eq. ~~1~~(1). To simplify the notation, the subscripts DI and overlines have been dropped from $\overline{m}_{\text{DI}}$, $\overline{\epsilon_{T,\text{DI}}}$ and $\overline{\epsilon_{U,\text{DI}}}$.

Variations in average thermal driving of the inflow at the ice front ($T_{\star\text{IF}}$) are strongly controlled by open-ocean dynamics and climate drivers, whereas ($\epsilon_T, \epsilon_U, \mu$) characterise the large-scale cavity dynamics, which is expected to depend on the cavity geometry. The relative importance of $T_{\star\text{IF}}$ and the transfer coefficients in controlling the temporal evolution of the melt rates as the cavity geometry evolves, will be assessed ~~next~~in section 4. To enable easy comparison between the different ~~factors on the right hand side of Eq. 1~~contributions, all quantities will be scaled by their respective values at $t = 0$:

$$\widetilde{m}(t) = m_0 \widetilde{\epsilon}_T(t) \widetilde{\epsilon}_U(t) \widetilde{\mu}(t)^2 \left(\widetilde{T}_{\star\text{IF}}(t) \right)^2 , \tag{13}$$

where $\widetilde{m}(t) = \frac{m(t)}{m(t=0)}, \widetilde{\epsilon}_T(t) = \frac{\epsilon_T(t)}{\epsilon_T(t=0)}$ ~~$\widetilde{m} = \frac{m}{m(t=0)}, \widetilde{\epsilon}_T = \frac{\epsilon_T}{\epsilon_T(t=0)}$~~, and so on.

To calculate the quantities in Eq. (13) or, equivalently, Eqs. (10) and (11), from model output requires a discrete version of the equations. In MITgcm, all variables in Eq. (10), including m, $U_\star$ and $T_\star$, are defined at cell centers of the Arakawa C grid, and spatial integrals directly translate into discrete sums. The calculation of $T_{\star\text{DI}}$ and $T_{\star\text{IF}}$ in Eq. (11) requires the evaluation of line integrals along the -400 m ice draft contours and ice fronts, respectively. Draft contours were calculated from the discrete MITgcm geometry, leading to a connected sequence of line segments with nodes that coincide with MITgcm nodes or the midpoint between MITgcm nodes. Ocean state variables and geometric variables were linearly interpolated to the midpoint of each line segment; velocities were subsequently projected to obtain the flow perpendicular to each segment. The contour integral was then replaced by a sum over all line segments, and quantities were evaluated at the center of each segment. For the calculation of $T_{\star\text{IF}}$ at the ice front, a similar procedure was followed, but contour nodes were taken directly from the Úa mesh. Further details on how each transfer coefficient was calculated from raw MITgcm output can be found on GitHub. A link to the code has been provided in the data availability statement at the end of the paper.

4 Ice-ocean feedbacks in the absence of far-field ocean variability

4.1 Evolution of melt rates and cavity geometry

A logical first step in the diagnosis of geometry-melt feedbacks in the deep interior of the Amundsen Sea cavities ~~,~~ is to simulate the response of the coupled ice-ocean system for suppressed temporal variability of the inflow at the ice front, i.e. $\widetilde{T}_{\star\text{IF}}(t) \approx 1$. In doing so, the time-dependency of normalized basal melt rates ($\widetilde{m}(t)$ in Eq. ~~13~~(13)) can be attributed solely to changes in the transfer coefficients, which capture changes in the cavity geometry, and any contamination from far-field ocean variability is eliminated. The experiments *hi_melt* and *av_melt*, described in Sect. 2.2, aim to achieve this by imposing time-invariant restoring conditions at the MITgcm boundaries for 200 years.

At the beginning of the *hi_melt* experiment, average basal melt rates in the deep interior range from 22.4 m yr^{-1} (Crosson) to 64.4 m yr^{-1} (Pine Island), as listed in Table 2. Corresponding melt rates for the *av_melt* experiment are between 12.6 m yr^{-1} and 54.3 m yr^{-1}. In both scenarios, pervasive thinning of all ice shelves causes significant inland migration of the grounding lines, as shown in Figure 4 for the *hi_melt* experiment, and Figure S1 for the *av_melt* experiment. The strongest retreat is concentrated along the central trunk of Pine Island Glacier, the Eastern Thwaites region, and Pope, Smith and Kohler East glaciers, which flow into the Crosson Ice Shelf.
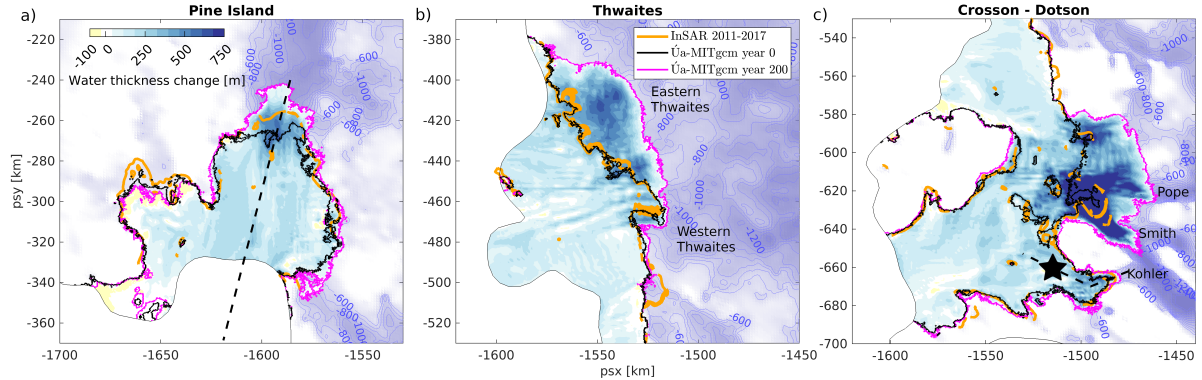
Figure 4. Change in water column thickness between years 0 and 200 of the *hi_melt* experiment. The Úa-MITgcm grounding line for both years is shown in black and magenta, respectively. For comparison, InSAR-derived grounding line locations between 2011 and 2017 (Rignot et al., 2016; Milillo et al., 2019, 2022) are shown in orange. Background colours and contours represent the bed topography (Morlighem et al., 2020). Dashed black lines in panels a and c correspond to the location of the thermohaline sections in Figure S2. The black star in panel c indicates the location of a bathymetric sill, discussed in Sect. 4.3

	Pine Island		Thwaites		Crosson		Dotson	
	hi_melt	*av_melt*	*hi_melt*	*av_melt*	*hi_melt*	*av_melt*	*hi_melt*	*av_melt*
$m(t=0)$ $\left[\text{m yr}^{-1}\right]$	64.4	54.3	46.4	40.9	22.4	12.6	27.3	21.3
$T_{\star\text{IF}}(t=0)$ [°C]	2.5	2.02	2.35	2.07	1.94	1.62	1.96	1.46
$\mu(t=0)$	1	1.15	1.22	1.26	1.18	1.03	0.95	1.06
$\epsilon_T(t=0)$	0.7	0.7	0.72	0.72	0.63	0.61	0.73	0.72
$\epsilon_U(t=0)\left[\text{m s}^{-1\circ}\text{C}^{-1}\right]$ $\epsilon_U(t=0)\left[\text{m s}^{-1}\text{K}^{-1}\right]$	0.002	0.0021	0.0011	0.0012	0.001	0.0011	0.0015	0.0018

Table 2. Average melt rates (m), thermal driving of the inflow across the ice front ($T_{\star\text{IF}}$), and transfer coefficients (μ, ϵ_T, ϵ_U) at time 0 for the deep interior cavities, defined as areas of the ice shelf with draft below -400 m (Fig. 3). Note that in agreement with Eq. (10), $m \approx m_0\epsilon_T\epsilon_U\mu^2\left(T_{\star\text{IF}}\right)^2$.

Concomitant with changes in the cavity geometry, average melt rates in the deep interior respond to geometrical changes in diverse ways, as can be seen from the top row in Figure 5. For the Crosson and Pine Island ice shelves, average melt rates in the

355 deep interior increase by as much as 75% and 35%, respectively. Average melt rates for the Dotson Ice Shelf decrease by up to 75%, whereas little to no changes occur for the Thwaites Ice Shelf. Whilst results for the *hi_melt* and *av_melt* simulations look broadly similar, the response of the latter is delayed due to the colder ocean thermal ~~forcing~~ driving and slower evolution of the cavity geometries.

In the next 4 ~~sections~~subsections, the physical ~~mechanisms~~ processes that cause the varied response of basal melt to changes

360 in ice-shelf geometry ~~will be explored. Specifically, the relationships between changes in cavity shape and different factors that determine the basal melt rate (thermal forcing~~ are explored. In particular, the evolution of the thermal driving at the ice front $(\widetilde{T}_{\star\mathrm{IF}}$~~, the outer cavity transfer coefficient~~) and 3 transfer coefficients ($\widetilde{\mu}$, ~~the thermal transfer coefficient $\widetilde{\epsilon}_T$ and the momentum transfer coefficient~~ , $\widetilde{\epsilon}_U$ ~~in Eq. 13) will be analysed in turn.~~) is analyzed one-by-one, allowing to draw general conclusions about the physical processes that control melt-geometry feedbacks, independent of the specific geometric characteristics of

365 each ice shelf. As will be shown in section 4.5, the momentum transfer coefficient $\widetilde{\epsilon}_U$ dominates the melt evolution, and a more in-depth analysis of the underlying dynamical causes is provided for each ice shelf.

4.2 ~~Thermal forcing~~ Limited change in thermal driving at the ice front

Due to the two-way coupling between ice-flux divergence and basal melt, a rich pattern of ice-shelf thickness changes develops, which evolves at a range of spatial and temporal scales. On average, the outer cavities in the *hi_melt* experiment expand

370 vertically by 10 to 15m per decade, or between 200 and 300m over the 200-year duration of the simulation, as shown in Figure 4. This is consistent with present-day rates of ice-shelf thinning (Paolo et al., 2015; Adusumilli et al., 2018). The evolving water column thickness and variable freshwater input at the ice-ocean interface are coupled to changes in ocean currents and stratification in the cavities. These feedbacks can lead to significant variability in thermal driving of the inflow at the ice front, despite the time-invariant restoring of ocean properties at the open boundaries of the domain, and despite

375 the absence of open-ocean surface fluxes. At the start of the *hi_melt* simulation, the average thermal ~~forcing~~ driving of the deep inflow across the ice front ($T_{\star\mathrm{IF}}(t=0)$) ranges from 2.5 °C and 2.35 °C for the Pine Island and Thwaites ice shelves, to 1.94 °C and 1.96 °C for the Crosson and Dotson ice shelves (see Table 2). Values for the *av_melt* experiment are typically 0.3-0.5 °C lower.

To diagnose changes in the thermal ~~forcing~~ driving of the cavity inflow and their impact on melt rates according to Eq.

380 ~~13~~(13), a time series of $(\widetilde{T}_{\star\mathrm{IF}})^2$ is depicted in the second row of Figure 5. All cavities experience notable variability up to 25% at a range of timescales. High-frequency fluctuations at monthly timescales are predominantly caused by Eddy activity at the ice front, which ~~occur~~ occurs irrespective of the changes in cavity geometry, as is apparent from identical simulations but with a fixed cavity geometry (not shown). ~~A detailed analysis of variability at sub(monthly) frequencies, including tidal variations, requires a higher sampling rate of the ocean data to avoid aliasing, and will not be pursued here.~~ At longer, decadal

385 to century timescales, trends in $(\widetilde{T}_{\star\mathrm{IF}})^2$ are small, except for a 20% and 10% increase for the Thwaites and Crosson ice shelves in the *hi_melt* experiment, and a 25%-30% reduction for Pine Island Ice Shelf in the *av_melt* experiment. The long-term trends
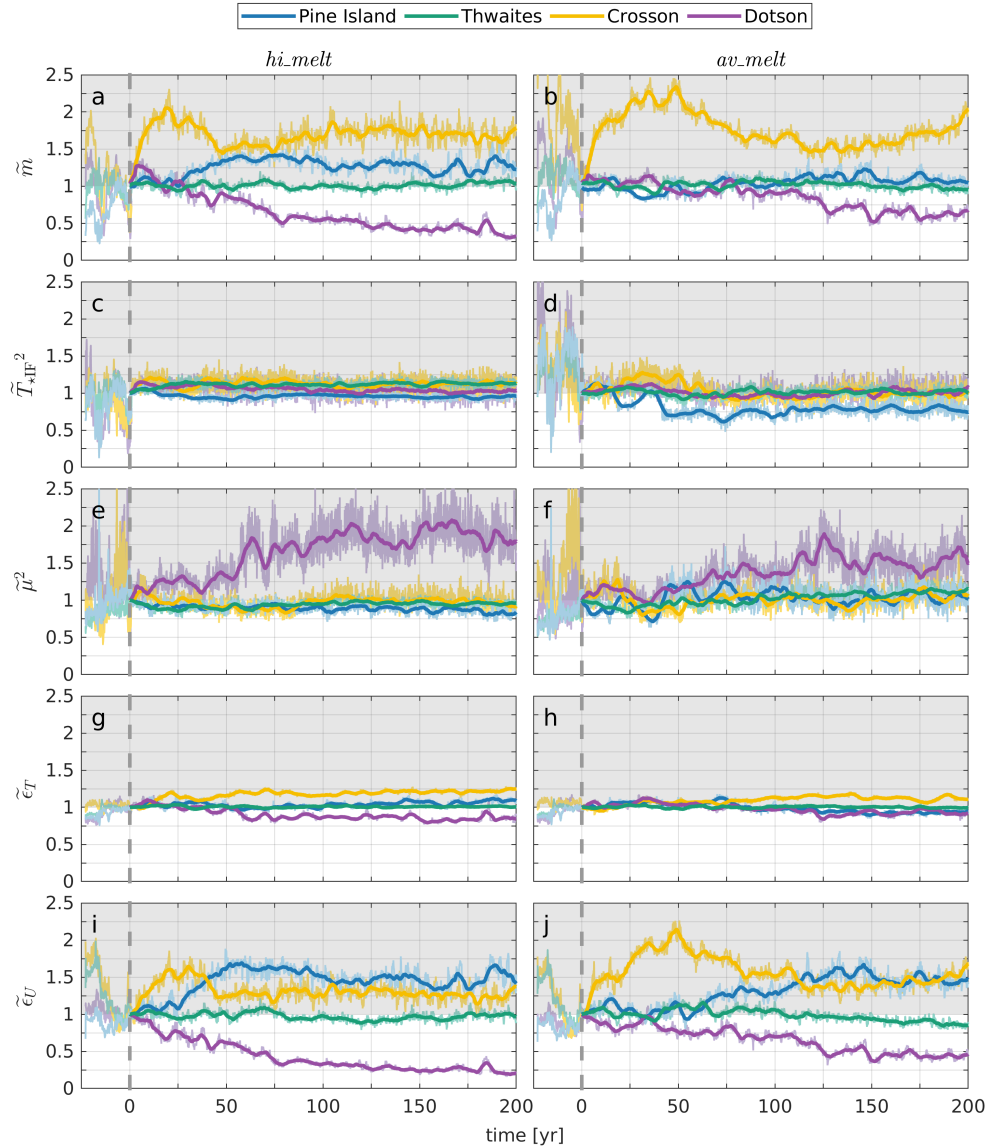
Figure 5. (a-b) Time series of average basal melt rates in the deep interior cavities for the *hi_melt* and *av_melt* experiments, normalized by values at time = 0. (c-d) Square of the normalized thermal ~~forcing~~ driving at the ice front, as defined in Eq. (12). (e-j) Time series of the normalized transfer coefficients, $\widetilde{\mu}$, $\widetilde{\epsilon}_T$ and $\widetilde{\epsilon}_U$, which link the thermal ~~forcing~~ driving at the ice front to melt rates in the deep interior according to Eq. (13). In all panels, thin lines correspond to monthly average values whilst overlaying thick lines correspond to a 5-year moving average. The dashed vertical line at time = 0 indicates the beginning of the *hi_melt* and *av_melt* experiments. Values at negative times correspond to an 18-year hindcast simulation with 1997-2014 ocean forcing, as described in App. A.

are a consequence of complex changes in cavity geometry, and difficult to attribute to individual processes. For example, the decrease in thermal ~~forcing~~ driving of Pine Island Ice Shelf coincides with a westward shift of the inflow pathways across the

ice front and vertical contraction of the mCDW core, in conjunction with a reduced cyclonic re-circulation in the upper water
390 column of the outer cavity, which adjusts to migrating channels in the underside of the ice shelf.

Overall, the connection between variability in $T_{\star\mathrm{IF}}$ and melt rates in the deep interior in the *hi_melt* and *av_melt* experiments
is weak. Indeed, if the time-varying factor $(\widetilde{T}_{\star\mathrm{IF}})^2$ in Eq. ~~13~~ (13) is replaced by its (constant) value at $t = 0$, the Root Mean
Square Error (rmse) between the resulting time series and $\widetilde{m}$ falls between 0.06 and 0.24 (see Fig. 6), which translates into
relative errors in average melt less than 15%. The only exception is Pine Island Glacier in the *av_melt* experiment with rmse =
395 0.34, which equates to a geometry-driven suppression of basal melt by 20-25%. Due to the overall small impact of changes in
$T_{\star\mathrm{IF}}$ on the melt rates in the deep interior, a detailed analysis of the processes that influence $T_{\star\mathrm{IF}}$ is not pursued here.
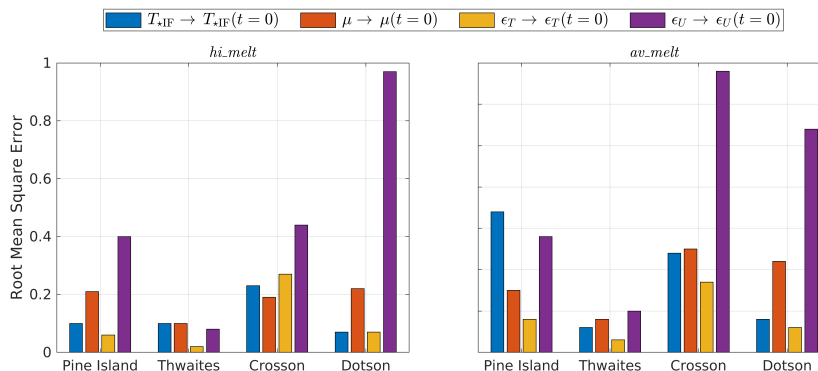
Figure 6. Root Means Square Errors (rmse) between $\widetilde{m}$ and the corresponding time series where a factor is replaced by its constant value
at t=0: $\mathrm{rmse}\,(\widetilde{m},\ \widetilde{m}\,(\mathcal{F} \to \mathcal{F}(t=0)))$, where $\mathcal{F}$ corresponds to $T_{\star\mathrm{IF}}$, μ, ϵ_T or ϵ_U. Rmse values provide an indication for how much of the
temporal variability in $\widetilde{m}$ can be attributed to each factor. Further details are provided in Sect. 4 of the main text.

4.3 ~~Outer~~ Geometrically constrained transport of water masses from the ice front to the interior cavity ~~transfer coefficient~~

Thermohaline properties of the cavity inflow do not invariably propagate into the deep interior. An aggregated measure for how
400 outer cavity processes can dampen or amplify changes in $T_{\star\mathrm{IF}}$ is provided by the ~~outer cavity transfer coefficient~~ *outer cavity*
transfer coefficient μ, defined in Eq. ~~11~~ (11). At time $t = 0$, values of μ are between 1 and 1.18 (Table 2), which implies that
~~the thermal forcing in the deep interior, $T_{\star\mathrm{DI}}$, is equal to or somewhat higher than $T_{\star\mathrm{IF}}$.~~ on average, water masses that reach
the deep cavity below -400 m have an equal or slightly higher thermal driving compared to water masses that cross the ice
front. The amplification of thermal driving can occur through the complex interplay between ocean dynamics and topography,
405 resulting in the blocking of water masses with lower thermal driving, which are typically found at shallower depths.

With time, however, dynamics of the coupled ice-ocean system causes μ to evolve in non-trivial ways. A time series of $\widetilde{\mu}^2$,
which is the quantity of relevance for the calculation of the normalized melt rates in Eq. ~~13~~ (13), is depicted in the third row of

Figure 5. Values higher (lower) than one correspond to an increased (decreased) connectivity between the ice front and deep interior compared to the start of the simulations. Two key observations can be made.

410 Firstly, in both forcing scenarios the Dotson Ice Shelf experiences a strong amplification of thermal driving in the deep interior as the cavity geometry evolves. Although the grounding line does not migrate by more than 2 km (Figs. 4 and S1) and shoals due to its retreat up a steep prograde bed slope (see Figure S2 for a vertical section along the black line in Figure 4c), the ice ~~draft~~ base rises by up to 300 m in places, which leads to a two-fold increase in water column thickness. As a result, the gap between the ice base and a bathymetric sill at the location indicated by the star in Figure 4c, is increased, which enables

415 more efficient transport of mCDW from the outer cavity into the deep interior (Fig. S2). This process, whereby shoaling of the ice draft enables warm waters to reach the grounding line, is similar to the mechanism that has been suggested to control the flow of mCDW towards the grounding line of Pine Island Glacier as it retreated from a bathymetric sill in the 1940s (De Rydt et al., 2014; Smith et al., 2017).

The second observation concerns the existence of high-frequency, monthly variability in $\widetilde{\mu}$, which is particularly evident

420 for the Dotson Ice Shelf. For all ice shelves, these short-term fluctuations are strongly anti-correlated with monthly changes in $\widetilde{T}_{\star \mathrm{IF}}$. The transfer coefficient μ therefore acts as a dampening factor for high frequency variability in the cavity inflow. Consequently, melt rates in the deep interior, as shown in Figure 5, are found to be relatively insensitive to short-term, Eddy-driven fluctuations of the thermal ~~forcing~~ driving at the ice front.

The overall impact of changes in the outer cavity transfer coefficient on basal melt rates in the deep interior can be assessed

425 by replacing the time-varying factor ($\widetilde{\mu}^2$ in Eq. ~~13~~(13)) by its value at $t = 0$. The rmse between the resulting timeseries and $\widetilde{m}$ are provided in Fig. 6, and fall between 0.08 and 0.25, which is equivalent to relative errors less than 10%. The only exception is the Dotson Ice Shelf, where the increase in thermal driving of the deep inflow causes a 50-60% increase in average basal melt when compared to conditions at the start of the simulations. However, it will be shown in Sect. 4.5 that despite the increase in ambient ocean thermal driving, melt rates of the Dotson Ice Shelf still decrease overall due to ~~changes in the mixed layer~~

430 ~~speed~~a reduction in the friction velocity relative to the ice base ($U_\star$ in Eq. (2)).

4.4 Thermal ~~transfer coefficient~~driving of the ice-ocean boundary layer and deep inflow are linearly related

The third coefficient to impact on average basal melt rates in the deep interior cavities is the *thermal transfer coefficient* ϵ_T, defined in Eq. ~~6~~(6) as the ratio between the thermal driving of the deep inflow ($T_{\star \mathrm{DI}}$ in Figure 3) and the thermal driving of the mixed layer adjacent to the ice-ocean interface ($T_\star$ in Figure 3). Values of ϵ_T at ~~$t = 0$ years~~ $t = 0$ vary between 0.7 and 0.73

435 for Pine Island, Thwaites and Dotson ice shelves (Table 2), and are somewhat lower for the Crosson Ice Shelf (0.61-0.63). Due to the input of cold freshwater at the ice-ocean interface, the thermal ~~forcing~~ driving of the mixed layer is strictly lower than that of the ambient ocean, or $\epsilon_T < 1$. It should also be noted that, for reasons that will be explored below, the value of ϵ_T is approximately independent of the forcing scenario.

In both simulations, the temporal variability of ϵ_T is less than $\pm 25\%$ (Fig. 5), with the largest changes found for the Crosson

440 and Dotson ice shelves. To understand the physical mechanisms that cause the increase or reduction of ϵ_T over time, it is instructive to analyze the relative importance, and underlying reasons, for variations in $T_{\star \mathrm{DI}}$ and $T_\star$. In Figure S3, a time series

of ϵ_T for the *hi_melt* experiment is compared to $T_\star/T_{\star\mathrm{DI}}(t=0)$ and $T_\star(t=0)/T_{\star\mathrm{DI}}$. It follows that for all ice shelves, except the Dotson Ice Shelf, variations in ϵ_T are dominated by changes in the thermal ~~forcing~~ driving of the mixed layer, $T_\star$. This can be understood as follows. For a given thermal ~~forcing~~ driving of the inflow, variations in $T_\star$ are strongly linked to changes in the gradient of the ice-shelf base, which controls the efficiency of turbulent entrainment of heat across the thermocline between the ambient water and mixed layer (Pedersen (1980); Jenkins (1991)). Indeed, as shown in Figure S3, changes in $T_\star/T_{\star\mathrm{DI}}(t=0)$ broadly track changes in the average gradient of the ice draft in the deep interior (∇b). The average basal gradient of the interior Crosson Ice Shelf cavity, for example, steepens from 0.034 to 0.054 during the 200-year *hi_melt* simulation. This coincides with a 28% increase in $T_\star$, whilst $T_{\star\mathrm{DI}}$ remains relatively constant and approximately equal to the thermal ~~forcing~~ driving at the ice front ($\widetilde{\mu}^2 \approx 1$ in Figure 5e). As a result, ϵ_T increases from about 0.62 to 0.78.

Whilst values of ϵ_T are generally linked to the slope of the ice draft and hence the cavity geometry, for the Dotson Ice Shelf changes in ϵ_T are dominated by the previously highlighted increase in thermal driving of the inflow ($\widetilde{\mu}^2 \gg 1$ in Figure 5e). During the first 50 years of the simulation, this coincides with a rise in ice draft and flattening of the ice-base gradients, as can be seen from the thermohaline section in Figure S2. In turn, this causes a concurrent reduction in thermal driving of the mixed layer (Fig. S3). Both increased thermal driving of the inflow and reduced thermal driving of the mixed layer cause the 20% reduction in ϵ_T, observed in Figure 5g.

Whilst the foregoing discussion was primarily focused on results from the *hi_melt* experiment, results from the *av_melt* experiment were found to be qualitatively similar, but delayed in time, as suggested by Figure 5h.

Despite a demonstrable link between changes in ice-shelf draft and ϵ_T, the relative impact of temporal variations in ϵ_T on basal melt rates in the deep interior is small. When the time-varying factor $\widetilde{\epsilon}_T$ in Eq. ~~13~~ (13) is replaced by its (constant) value at $t=0$, the rmse between the resulting timeseries and $\widetilde{m}$ falls between 0.02 and 0.17 (see Fig. 6), or a relative error in average basal melt rates less than 10%. The only exception is the Crosson Ice Shelf, with a rmse = 0.27, or a relative error around 20%.

4.5 ~~Momentum transfer coefficient~~ Changes in cavity circulation dominate melt rate evolution

The fourth and final coefficient ~~to control~~ controlling average melt rates in the deep interior is the ~~momentum transfer coefficient~~ *momentum transfer coefficient* ϵ_U, which links the mixed layer velocity to the thermal driving of the inflow (Eq. ~~7~~ (7)). At decadal timescales, changes in ϵ_U dictate the majority of variability in the melt rates, as is apparent from the strong similarities between $\widetilde{\epsilon}_U$ and $\widetilde{m}$ in Figure 5. Since the temporal variability in thermal driving of the deep inflow is relatively small – the Dotson Ice Shelf being the only exception – changes in ϵ_U are dominated by variability in the mixed layer friction velocity $U_\star$. This is demonstrated in ~~Figure S4~~ Figure S4, which shows a strong agreement between ϵ_U and $U_\star/T_{\star\mathrm{DI}}(t=0)$, whereas the similarity to $U_\star(t=0)/T_{\star\mathrm{DI}}$ is much weaker.

Based on a general scaling analysis, Holland et al. (2008) argued that for a given cavity geometry, $U_\star$ depends approximately linearly on the far-field thermal ~~forcing~~ driving. Results from the *hi_melt* and *av_melt* experiments suggest that the linear scaling factor, ϵ_U, is strongly dependent on the geometry of the cavity. Whilst no studies have considered this dependency in detail, insights from 2D plume theory ~~(Lazeroms et al. (2019))~~ (Lazeroms et al., 2019) and numerical ocean simulations for simplified ice-shelf shapes ~~(Holland et al. (2008))~~ (Holland et al., 2008) suggest that ϵ_U is a monotonically increasing function
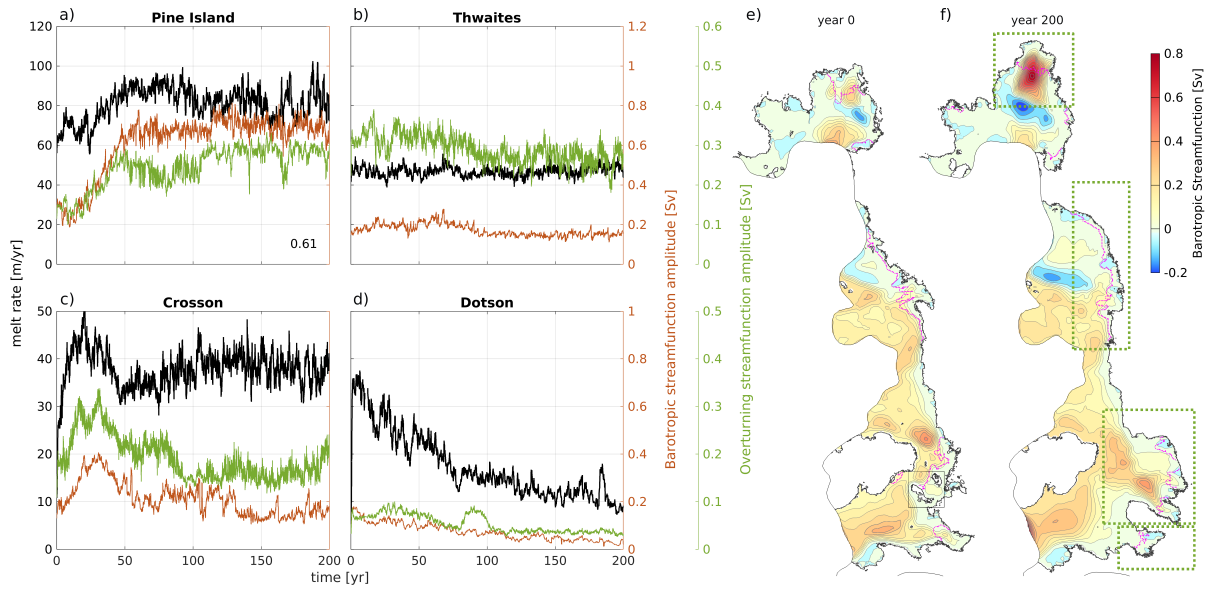
Figure 7. (a-d) Average melt rates in the deep interior cavities (black lines, left y-axis) are shown alongside the barotropic and overturning streamfunction amplitudes (red and green lines, right y-axis, note the different limits). The latter are calculated from the meridional (Pine Island) and zonal (Thwaites, Crosson, Dotson) transport within the boxes outlined by green dashed lines in panel f. R-values correspond to the correlation coefficient between mean melt rates and barotropic streamfunction amplitudes. (e-f) Barotropic streamfunction at years 0 and 200. Magenta lines delineate the boundaries of the deep interior cavities, i.e. areas with ice-shelf draft below -400 m. All plots are based on the *hi_melt* experiment.

of the gradient of the ice base. However, analysis of the *hi_melt* and *av_melt* experiments does not support such a monotonically increasing relationship. Instead, the two quantities are found to be weakly anti-correlated (not shown), indicating that ϵ_U cannot be quantified in terms of the geometry of the ice base alone, and furthermore, spatially averaged ice-shelf basal gradients only play a subsidiary role in controlling the ~~mixed layer~~ friction velocity, $U_\star$, at least for the complex geometries presented here.

480 ~~Whilst basal gradients do locally impact on~~ To understand how $U_\star$ (and therefore ϵ_U and melt rates m) vary with changes in cavity geometry, it is instructive to analyze the barotropic and overturning components of the cavity circulation. The time evolution of the barotropic streamfunction amplitude is shown in Figure 7a-d. The streamfuction amplitude, which is defined as the difference between the maximum and minimum value of the barotropic streamfunction in the deep interior (delineated by the magenta lines in Figure 7e-f) is a measure for the strength of the horizontal transport within the cavity. Figure 7a-d

485 shows that over time, the strength of the horizontal circulation in the Pine Island and Dotson ice shelf cavities increases and decreases, respectively. On the other hand, no significant changes in the barotropic flow are simulated beneath Thwaites Ice Shelf, whereas the circulation in the Crosson Ice Shelf cavity first increases and subsequently reduces. Figure 7a-d also shows that variations in the barotropic streamfunction amplitude closely track changes in average basal melt rates.

Together with the variability in horizontal transport, changes in basal meltwater production dominate the buoyancy-driven overturning circulation of the Amundsen cavities, as noted previously by Jourdain et al. (2017). For each cavity, a measure of the overturning strength was obtained from the meridional (Pine Island) or zonal (Thwaites, Crosson, Dotson) overturning streamfunction amplitude, calculated for the areas enclosed by the boxes with dashed lines in Figure 7e. Timeseries of the overturning streamfunction amplitude in Figure 7a-d indeed show temporal variability that is comparable to changes in the barotropic streamfunction amplitude and basal melt rates. It is important to reiterate that, whilst gradients of the ice base do locally affect the buoyancy of the mixed layer and influence horizontal pressure gradients that determine the ~~geostrophic flow (Jenkins, 2016), the depth-average circulation is additionally~~ vertical shear, changes in the average basal gradient of the deep interior ice shelves (see Fig. S3) do not correlate with changes in the overturning amplitude or average melt rates.

The above results suggest that extensive geometrical changes, which unfold over multi-annual to decadal timescales, can induce persistent adjustments to the large-scale horizontal and overturning circulation within the cavity. This coincides with comparable changes in the mixed layer friction velocity $U_\star$ and hence the melt rates. To understand how changes in cavity geometry and circulation are connected, one should recall that the barotropic circulation is constrained by the conservation of barotropic potential vorticity, ~~henceforth referred to as~~ or BPV (Patmore et al. (2019) or Bradley et al. (2022)). ~~To~~ This implies that, to leading order, the depth-averaged flow aligns with contours of constant $\frac{f+\zeta}{H}$, where f is the Coriolis parameter, which is approximately constant for the region of interest, ζ is the depth-averaged relative vorticity, and H is the spatially variable water column thickness. ~~As a result, the depth-averaged currents are strongly constrained by the (temporally evolving)~~ Over time, the temporally evolving water column thickness can induce significant changes to the spatial distribution of BPV, and hence the 3D ~~geometry of the cavity~~ structure of the circulation.

~~An example of how the BPV and depth-averaged cavity circulation of Pine Island Ice Shelf co-evolve~~ Whilst the discussion above was based on results from the *hi_melt* experiment, panel j in Figure 5 shows that an equally significant relationship between ϵ_U (and hence $U_\star$) and melt rates exists for the *av_melt* experiment. The dominant impact of geometrically induced changes in cavity circulation on the melt rates is therefore independent of the specific realization of far-field ocean forcing used in the *hi_melt* ~~experiment is provided in Figure S5. With time, BPV generally becomes~~ and *av_melt* experiments. The only key difference is the timescale at which those geometry-melt feedbacks unfold. Compared to the *hi_melt* experiment, the cavity geometries in the *av_melt* evolve more slowly due to the lower ocean thermal forcing, which causes an associated delay in the melt-rate response.

Given the important links between changes in cavity geometry, circulation and basal melt, a more detailed account of the feedbacks for individual ice shelves is provided below.

Pine Island Ice Shelf:
Changes in cavity circulation result in a 75% increase of ϵ_U during the first 60 years of the simulation (Fig. 5i) followed by relatively constant values of ϵ_U. This coincides with a 3-fold increase and levelling off of the barotropic and overturning streamfunction amplitudes (Figure 7a) and a 50% increase in basal melt rates.

The Pine Island Ice Shelf provides a clear example of how BPV and the depth-averaged cavity circulation co-evolve over time. During the first 60 years of the *hi_melt* simulation, BPV in the deep interior cavity becomes generally less negative due to ~~the~~ an increase in water column thickness H, as shown in Figure S5. At all times, no continuous contours of BPV exist that link the outer cavity to the deep interior, in part due to the existence of a prominent bathymetric sill that extends north-to-south (left-to-right in the figure) around $x = 300$ km (Jenkins et al., 2010). As a result, there are no direct pathways of barotropic flow between the outer cavity and deep interior that conserve BPV, and the cavity circulation is divided into two cyclonic gyres (one in the deep interior, one in the outer cavity) separated by an anticyclonic current on the seaward side of the sill. ~~The same current structure~~This current structure, which is illustrated by the barotropic streamfunction in Figure 7e at year 0, was previously reported by Dutrieux et al. (2014) and Bradley et al. (2022). As the grounding line retreats between years 0 and 60, the area with continuous contours of BPV landward of the sill doubles in size (the region indicated by the box with dashed lines in Figure S5), which allows the cyclonic gyre to laterally expand. At the same time, the strength of the gyre increases from about 0.25 Sv to 0.65 Sv, sustained by the almost 2-fold increase in meltwater production (and associated increase in buoyancy) in the cavity interior, from 50 Gt yr^{-1} to 90 Gt yr^{-1}. The expansion and strengthening of the gyre is illustrated by the barotropic streamfuction for year 200 in Figure 7f. As the Pine Island grounding line retreats, the average gradient of the ice base does not significantly change (see section in Figure S2 along the dashed line in Figure S3a). Instead, the increase in meltwater production is enabled by, and sustained by, changes in the ~~depth-averaged cavity circulation.~~

~~(a-d) Average melt rates (black lines, left y-axis) and average ocean current speed (green lines, right y-axis) in the deep interior cavities are shown alongside the barotropic and overturning streamfunction amplitudes (orange and yellow lines, right y-axis). The latter is calculated from the meridional (Pine Island) and zonal (Thwaites, Crosson, Dotson) transport within the boxes outlined by yellow dashed lines in panel f. R-values correspond to the correlation coefficient between mean melt rates and average current speed. (e-f) Barotropic streamfunction at years 0 and 200. Magenta lines delineate the boundaries of the deep interior cavities, i.e. areas with ice-shelf draft below -400 m. All plots are based on the *hi_melt* experiment.~~

~~A more general analysis of the *hi_melt* and *av_melt* experiments shows significant temporal variability of the depth-mean flow in~~ large-scale barotropic and overturning circulation within the deep interior~~of all cavities, as demonstrated in Figure 7 for the *hi_melt* experiment. Furthermore, a strong linear relationship exists between the depth-mean flow and the mixed layer speed, $U_\star$, and hence ϵ_U. For the Pine Island Ice Shelf, a 75% increase of ϵ_U during the first 60 years of the simulation (Fig. 7a) followed by relatively constant values of ϵ_U, coincides with a 2-fold increase and levelling off of the depth-mean flow, consistent with the discussion above. Both time series are positively correlated with correlation coefficient 0.82. .~~

Thwaites Ice Shelf:

For the Thwaites Ice Shelf, neither ϵ_U nor the ~~average depth-mean flow~~ barotropic and overturning circulation display any significant variability over the duration of the simulations (Figure 7b). As a result, average basal melt rates in the deep interior cavity remain approximately constant. This does not contradict results from Holland et al. (2023), as the simulations presented here do not include the same detailed retreat of the Western Thwaites Ice Tongue. Instead, at the start of the simulations, the Thwaites grounding line has already retreated past the pinning point that was highlighted by Holland et al. (2023) as

the main geometric control on basal melt rates of the Thwaites Ice Tongue. The lack of any strong geometrical feedbacks can be explained by the shallow (> -900 m) and relatively featureless bedrock topography over which the Eastern Thwaites grounding line retreats (Fig. 4). A narrow band of relatively low melt rates (< 50 ~~myr~~m yr^{-1}) tracks the moving grounding line (not shown) without significant modification to the geometrical configuration and ~~currents.~~ current speed. This might change once the grounding line of the western Thwaites Glacier retreats inland from the subglacial ridge it is currently pinned on. However, this does not occur over the 200-year duration of the simulations presented here.

Crosson Ice Shelf:

For the Crosson Ice Shelf, a sharp increase and decline of ϵ_U during the first 50 years (Figure 5i) is followed by approximately constant values for the remainder of the simulation. This coincides with equivalent changes in the ~~depth-average flow (correlation coefficient 0.73)~~ barotropic and overturning streamfunction amplitudes in Figure 7c. The sharp increase in flow speed, and subsequent decline, are linked to the ungrounding of several large ice rises downstream of the main grounding line of Smith Glacier, indicated by the black box near the bottom of Figure 7e. The removal of these topographic barriers causes a reorganisation of the cavity circulation and melt rate distribution, which stabilizes after about 50 years, and the Smith Glacier continues its retreat into a deep, narrow trough ~~. Finally, the~~ without further significant changes to the current structure.

Dotson Ice Shelf:

The gradual 4-fold decrease in ϵ_U for the Dotson Ice Shelf (Figure 5i) coincides with a 4-fold reduction in the ~~depth-average flow~~ barotropic and overturning streamfunction amplitude, as shown in Fig. 7d (correlation coefficient 0.97). The slow-down of the circulation is largely explained by the loss of buoyancy, as the grounding line retreats up a prograde bed slope and the ice draft rises above the thermocline in most places ~~(Fig.~~. This process is illustrated in the top row of Fig. S2 ~~)~~.

~~An alternative way to analyze changes in the large-scale cavity circulation is through the barotropic streamfunction. The latter is presented in Figure 7 at $t = 0$ and 200 years, and corroborates the strengthening of the cyclonic gyre in the deep interior cavity of Pine Island Glacier, the relatively unchanged strength of the depth-integrated transport beneath the Thwaites Ice Shelf, a modest increase in circulation in the deep interior of the Crosson Ice Shelf cavity, and significant weakening of the circulation in the Dotson Ice Shelf cavity. Furthermore, the barotropic streamfunction amplitude, defined as the difference between the maximum and minimum value of the streamfunction in the deep interior (delineated by the magenta lines in Figure 7e-f) closely tracks the variability in ϵ_U, as shown in panels a-d in Figure 7.~~

~~Together with the variability in horizontal transport, changes in basal meltwater production modulate the buoyancy-driven overturning circulation of the Amundsen cavities, as noted previously by Jourdain et al. (2017). Similar conclusions apply here. For each cavity, a measure of the overturning strength is obtained from the meridional (Pine Island) or zonal (Thwaites, Crosson, Dotson) overturning streamfunction amplitude, calculated for the areas enclosed by the boxes with dashed lines in Figure 7e. Timeseries of the baroclinic streamfunction, as shown in Figure 7a-d, indeed show temporal variability comparable to that of the barotropic streamfunction amplitude, with correlation coefficients $R = 0.84$ (Pine Island), $R = 0.57$ (Thwaites), $R = 0.73$ (Crosson) and $R = 0.78$ (Dotson).~~

Finally, as can be seen from panel j in Figure 5, results for the *av_melt* experiment are qualitatively similar, and are not explored in detail here. The only key difference compared to the *hi_melt* experiment is a delay in the melt-rate response due to the lower ocean thermal foreing and slower evolution of the cavity geometries.

5 The importance of far-field ocean variability

So far, geometrically driven geometrically-driven changes in basal melt have been discussed in the context of suppressed variability of the far-field ocean. In reality, interannual to multi-decadal shifts in ocean conditions, linked to internal climate variability and anthropogenic trends in the atmosphere, are understood to be important regulators of ice-shelf melt in the Amundsen Sea. Aided by repeat measurements of ocean properties on the continental shelf, significant progress has been made in understanding the links between natural climate variability, including tropical ENSO activity, and decadal variations in basal melt (Jenkins et al. (2016) and reference therein, Silvano et al. (2022)). On the other hand, the impact of past and future anthropogenic climate change on ice-shelf melt in the Amundsen Sea has only recently started to be addressed (Naughten et al., 2022; Jourdain et al., 2022a). In all cases though, the interplay between different modes of far-field ocean variability and geometrically-driven changes in melt rates has not been included in numerical simulations in global (Timmermann and Hellmer, 2013; Naughten et al., 2018; Siahaan et al., 2022) and regional (Naughten et al., 2022; Jourdain et al., 2022a) ocean model setups with thermodynamically active ice shelf cavities. Of the studies above, only Siahaan et al. (2022) included a dynamically evolving ice sheet. However, the 1° resolution of their global ocean configuration was too coarse to reliably capture the spatial distribution of melt rates beneath the small Amundsen Sea ice shelves. In this section, a first step is taken towards addressing this shortcoming. In particular, the combined impact of naturally occurring (present-day) ocean variability in the Amundsen Embayement Sea Embayment and geometrically-driven changes in melt rates is considered at a much higher horizontal resolution (1.3 km) than previously achieved. Uncertain anthropogenic trends in regional ocean conditions are not included here, but are the subject of a forthcoming study.

To compare geometrically driven geometrically-driven changes in melt to changes caused by interannual to decadal variations in far-field ocean conditions, two numerical experiments were conducted, *ref_melt* and *var_melt*, as described in Sect. 2.2. In the *ref_melt* experiment, the ocean state was restored at the eastern and northern open boundaries to monthly average conditions over a an 18-year period (01/1997-12/2014), repeated 11 times, whilst the cavity geometry was kept fixed to its present-day configuration (see App. A for details about the geometry). A 5-year moving average of mean melt rates in the deep interior cavities, shown in Figure 8, displays 11 near-identical cycles with interannual variability ranging from 20% (Thwaites) to 50-60% (Pine Island and Dotson) and 80% (Crosson). The results for fixed ice-shelf cavities are plotted alongside results from the *var_melt* experiment, which imposes the same oceanographic restoring conditions but additionally includes evolving cavity geometries. Three broad conclusions can be drawn.

1. The basal melt variability in the *var_melt* experiment consists of interannual changes superimposed onto a (multi)decadal trend. The latter is absent from the *ref_melt* experiment, but closely resembles the long-term variability in the *av_melt* experiment (orange red line in Figure 8), providing evidence for its geometrical origin. Results demonstrate suggest that
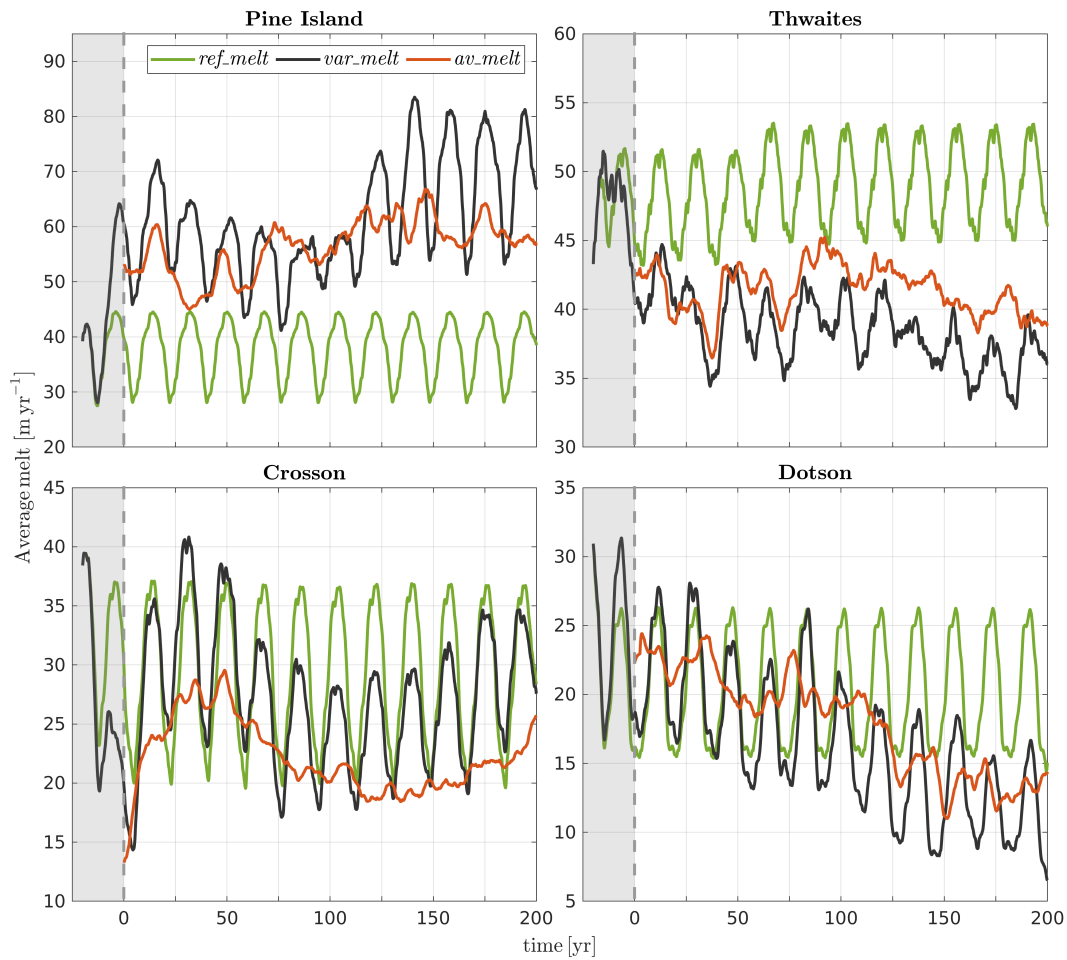
Figure 8. Five-year moving average of melt rates in the deep interior cavities for the *ref_melt* experiment (cyclic restoring of 1997-2014 ocean boundary conditions with static cavities), the *var_melt* experiment (cyclic restoring conditions with evolving cavities), and the *av_melt* experiment (constant restoring conditions with evolving cavities).

whilst basal melt variability is dominated by internal climate variability at decadal timescales, changes in cavity geometry can play a non-negligible role at longer timescales. In particular, it should be noted that the impact of geometrical feedbacks can cause both a long-term amplification of basal melt, as is the case for the Pine Island Ice Shelf, and a long-term suppression of basal melt, as is the case for the Dotson Ice shelf.

2. Interannual changes caused by far-field ocean variability and multi-decadal trends caused by geometrical feedbacks are not independent. Indeed, the amplitude of interannual melt variability differs between individual 18-year cycles in the *var_melt* experiment, which indicates that the sensitivity of melt rates to (inter)annual changes in far-field ocean conditions depends on the cavity geometry. This is particularly evident for the Pine Island Ice Shelf, showing lower

625

amplitude variations in years 75-115, compared to, e.g., years 125-200. Whilst average melt rates scale approximately quadratically with the thermal driving of the inflow within each 18-year cycle (not shown), the scaling factor does not remain constant between cycles. This is consistent with the results presented in Sect. 4, which highlighted the strong dependency of the scaling factor ($\mu^2 \epsilon_T \epsilon_U$ in Eq. ~~1~~(1)) on the cavity geometry.

3. For the Pine Island and Thwaites ice shelves, the envelope of melt variability in the *var_melt* experiment falls outside the range of variability in the *ref_melt* experiment, underlining the dominant impact of geometrical feedbacks on the melt rates. Over the 200-year duration of the experiments, the average difference between the *var_melt* and *ref_melt* melt time series is 22 ma^{-1} or 58% for the Pine Island Ice Shelf, -9.4 ma^{-1} or -19% for the Thwaites Ice Shelf, -2.3 ma^{-1} or -8% for the Crosson Ice Shelf and -3.3 ma^{-1} or -16% for the Dotson Ice Shelf. In all cases except for the Pine Island Ice Shelf, simulations that ignore geometrical feedbacks overestimate future melt rates forced by present-day ocean conditions. It remains to be shown that this conclusion holds in simulations with realistic atmosphere-ocean interactions and for weaker ocean restoring conditions that allow complex feedbacks between meltwater production, sea ice production and water mass properties on the continental shelf~~(Jourdain et al., 2017)~~.

6 Glaciological implications

A prime objective of the preceding analysis was to identify potential feedbacks in the ice-ocean system, whereby grounding line retreat triggers changes in ocean dynamics with lasting implications for the ice-shelf mass balance, independent of the far-field ocean conditions. Whilst the focus has been on the response of ocean-driven melt to changes in cavity geometry, the impact of geometrical feedbacks on the net mass balance of the ice shelves, including grounding line fluxes, needs to be considered in order to assess their importance for the future dynamics of the Antarctic Ice Sheet.

In broad agreement with the observational record (Depoorter et al., 2013), ice shelves in the Úa-MITgcm 1997-2014 hindcast simulation (Appendix A) have a negative net mass balance between -40 Gt yr^{-1} and -10 Gt yr^{-1}, as shown by the black line for negative times (grey shaded area) in Figure 9. The interannual variability in mass changes during the hindcast period arises predominantly from changes in ice-shelf basal melting (solid ~~an~~ and dashed blue lines in Fig. 9) due to variations in the thermocline depth of the far-field ocean forcing. The corresponding variations in grounding line discharge (red line) and ice front flux (orange line) during the hindcast period have a much lower amplitude.

It is prudent to recall that in all simulations, the surface mass balance (SMB, green lines) was kept constant and equal to a 1979-2015 climatology (van Wessem et al., 2018). While this assumption might not be valid in century-scale projections, present-day surface accumulation only contributes a small fraction of the total ice-shelf mass balance in the region, and any impact of temporal variability on the net mass balance of the ice shelves will be disregarded. Furthermore, the ice front was fixed to its 1997 location, even though variations in ice-shelf extent and associated changes in buttressing have been shown to impact on the ice-shelf mass balance in recent years (Joughin et al., 2021; Bradley et al., 2022). Equally, changes in ice-shelf rheology, including rifting and fracturing, have been ignored, despite their importance for ice-shelf and ice-sheet dynamics in the region (De Rydt et al., 2021; Surawy-Stepney et al., 2023).
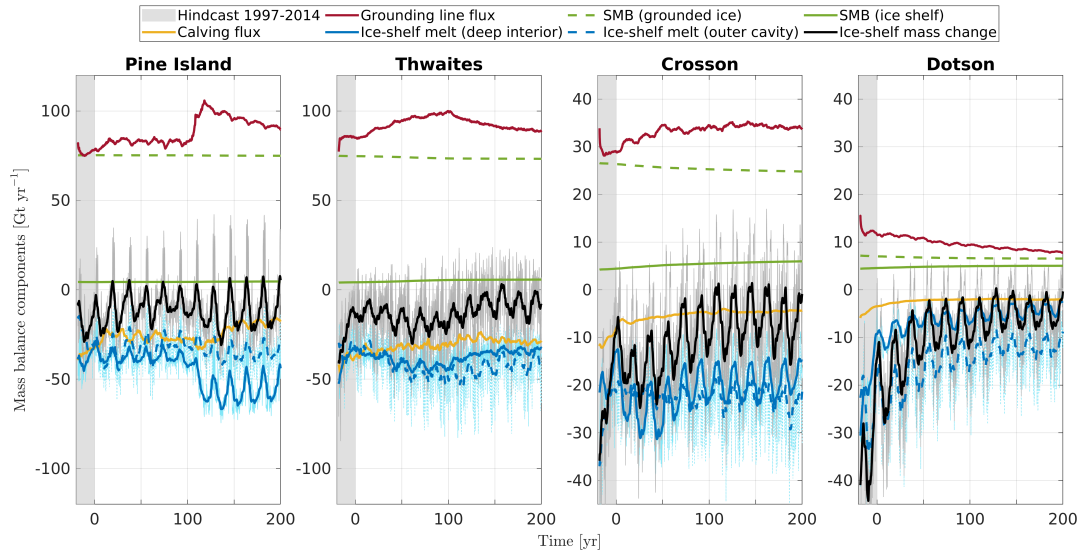
Figure 9. Temporal evolution of integrated mass balance components in the hindcast experiment (grey shaded area, see Appendix A for details) and the *var_melt* experiment (0 to 200 years, see Sect. 2.2 for details). Ice-shelf mass changes (black curve) are equal to the sum of the grounding line flux (red curve), surface mass balance (SMB, solid green curve), calving flux (orange line), ice-shelf melt in the deep interior (solid blue line), and ice-shelf melt in the outer cavity (dashed blue line). For reference the SMB of the grounded ice is represented by the dashed green line and is lower than the grounding line flux, indicating net mass loss (or positive sea-level contribution) from each glacier basin.

The focus in the remainder of this section will be on results from the *var_melt* experiment. Through repeat forcing of present-day decadal variability in ocean conditions and the inclusion of evolving cavity geometries, results from this simulation capture
665 the combined impact of decadal ocean variability and geometrical feedbacks on the net mass balance of the ice shelves. Similar results for the *hi_melt* experiment with fixed ocean boundary conditions are provided in Figure S6, and will be discussed briefly at the end.

Results in Fig. 9 show that between years 0 and 200, the net mass balance of all ice shelves remains negative under the imposed ocean and atmospheric conditions. Only during intermittent episodes of 1 to 5 years does lower-than-average basal
670 melting cause a positive net mass balance. Such episodes of positive net mass balance occur more frequently towards the end of the simulation, when ice-shelf mass changes tend to less negative values for the Thwaites, Crosson and Dotson ice shelves. Broadly speaking, fluctuations in basal mass loss, both in the deep interior and outer cavities (solid and dashed blue lines in Fig. 9, respectively) dominate the variability in the net mass balance of the ice shelves at decadal timescales. The amplitude of variations in grounding line flux, surface mass balance and ice front (or calving) fluxes is significantly lower.
675 At longer timescales, however, significant shifts in grounding line flux occur. One notable example is the rapid, 40% increase in grounding line discharge of Pine Island Glacier between years 100 and 120. For other ice shelves, changes in mass influx across the grounding line evolve more gradually, at least in the *var_melt* experiment, with a 25% (0.2 Gt yr^{-2}) increase over

100 years for the Thwaites Ice Shelf, a 15% (0.1 Gt yr^{-2}) increase over 50 years for the Crosson Ice Shelf, and a gradual 30% (0.02 Gt yr^{-2}) decline over 200 years for the Dotson Ice Shelf.

680   Without a compensating response of other components of the ice-shelf mass balance, the increase in grounding line flux for Pine Island, Thwaites and Crosson ice shelves would imply a smaller negative, or even positive net mass balance. For the Pine Island Ice Shelf in particular, the 40% (or 30 Gt yr^{-1}) increase in grounding line flux would lead to a persistently positive net mass balance, causing the ice shelf to thicken and enable the glacier to readvance. Instead, the abrupt change in grounding line flux is largely compensated for by a shift in basal mass loss in the deep interior cavity, which enables the sustained thinning of

685   the ice shelf and associated retreat of the grounding line. Similar findings apply to the other ice shelves: multidecadal trends in grounding line flux are largely compensated for by shifts in basal mass loss with similar magnitude but opposite sign. While changes in ice-front discharge occur too, they manifest themselves at longer timescales, and their general decline tends to shift the net ice-shelf mass balance towards more positive values, rather than counteract the changes in grounding line flux.

The finding that melt rates play an important role in sustaining the negative mass balance of the ice shelves despite significant

690   changes in grounding line flux, is not new. However, the physical mechanisms by which it does so, have not previously been studied in detail. In particular, mechanisms that enable sustained adjustments in basal mass loss that occur independent of the external forcing, have not been explored. In this study, the close interaction between changes in cavity geometry, ocean circulation and basal melt has been identified as a candidate for such a mechanism. For example, based on the analysis in preceding sections, the 60% increase in meltwater flux in the deep interior of the Pine Island Ice Shelf cavity between 100 and

695   120 years, is enabled by a strong adjustment of the barotropic flow in response to changes in the cavity geometry. At the point where no further geometry-driven changes in circulation and melt rate occur, an increasing mass flux across the grounding line cannot be accommodated without causing a less negative or positive net ice-shelf mass balance. As a result, ice-shelf thinning and grounding line retreat is either slowed down ,or prevented. Results from the *var_melt* experiment indicate that this is more generally true: peaks in grounding line discharge coincide with a maximum in ice-shelf basal mass loss for all ice shelves,

700   except the Dotson Ice Shelf. The evolution of the latter is somewhat different, as it experiences a gradual decline in grounding line flux, despite a persistent negative net mass balance of the ice shelf. Changes in grounding line flux are small, however, compared to the strongly negative trend in basal mass loss, which drives the net mass balance towards zero. The 75% reduction in basal melt rates is again linked to changes in cavity geometry, as argued in Sect. 4, and drives the system towards a new equilibrium state with the grounding line of the tributary Kohler West Glacier (Fig. 4) located on a prominent bathymetric sill

705   (Fig. S2).

Broadly similar conclusions can be drawn from the *hi_melt* experiment (Fig. S6) and the *av_melt* experiment (not shown). For both simulations, despite the absence of temporal variability in ocean forcing, sudden or gradual increases in grounding line discharge into the Pine Island, Thwaites and Crosson ice shelves are largely compensated for by an increase in ice-shelf basal mass loss. Based on the analysis in preceding sections, such changes in basal melt can be linked to an adjustment of

710   the cavity circulation in response to changes in the cavity geometry. Melt-geometry feedbacks therefore enable a sustained negative net mass balance of the ice-shelves, and promote ongoing retreat of the grounding line, independent of the far-field oceanographic conditions. As a final comment it is worth noting that whilst this mechanism operates under current glaciological

conditions, dynamical instabilities such as the marine ice sheet instability (Weertman, 1974, e.g.), can cause sustained retreat of the grounding line, independent of the amount of basal mass loss. However, no evidence for such a mechanism was detected here.

7 Summary and conclusions

Numerical simulations with a high resolution coupled ice-ocean model were used to quantify the connection and feedbacks between changes in cavity geometry and basal melting of ice shelves in the Amundsen Sea Embayment, West Antarctica. Under a range of present-day ocean conditions, sustained thinning of the Pine Island, Thwaites, Crosson and Dotson ice shelves was shown to cause pervasive retreat of the grounding lines by up to 50 km over a 200-year period. For each ice shelf, ~~the resulting changes in geometry were linked to~~ extensive changes in cavity geometry led to persistent dynamical adjustments of the ~~cavity~~ ocean circulation, and to ~~strong and varied~~ opposing changes in basal melt near the grounding lines. In particular, a significant correlation was found between the geometrical amplification (e.g. Pine Island) or suppression (e.g. Dotson) of the ~~barotropic~~ cavity circulation, and the up-to 75% increase (Pine Island) or 75% decrease (Dotson) in average basal melt rate~~, irrespective of the~~. The main conclusions and implications are summarized as follows.

At multi-annual to decadal timescales, feedbacks between ice-shelf geometry and basal melt rates are dominated by changes in the friction velocity at the ice base ($U_\star$). A much smaller proportion of the variability is explained by geometrically-induced changes in thermal driving at the ice base. Simulated changes in $U_\star$ are dynamically linked to variability in the barotropic and overturning circulation, whilst no significant relationship was found between changes in melt and simple geometric characteristics of the ice shelf, such as the depth or gradient of the ice base. The changes in melt are therefore controlled by complex adjustments of the ocean dynamics to the 3D evolution of the cavity geometry. This has important implications for commonly-used parameterizations of basal melt, which are typically calibrated for present-day ice-shelf geometries and depend on (local) gradients and/or depth of the ice base alone. Since these parameterizations do not account for the effects of changes in cavity circulation, their application to geometrically complex settings over timescales that allow significant adjustments of the water column thickness, should be carefully tested. The results in this study suggest that the timescales over which geometrical feedbacks dominate the melt variability can be as short as several decades.

The physical processes that control melt-geometry feedbacks operate irrespective of the far-field ~~ocean forcing. The geometry-induced shifts in basal ablation were found to manifest themselves at decadal to multidecadal timescales , and outweigh, in some cases, variations in melt rates that occur~~ ocean forcing, although the latter have a strong impact on the timescales over which the feedbacks unfold. While results suggest that internal climate variability dominates the basal melt variability in the Amundsen Sea over multi-annual timescales, rapid and extensive adjustments of the cavity circulation over decadal timescales can lead to sustained changes in melt that outweigh variations due to natural variability in far-field ocean ~~conditions. The newly-identified geometry-melt feedbacks~~ properties. Importantly, simulations with a static cavity geometry can lead to a systematic positive or negative bias in melt rate projections by up to 75% compared to simulations that include a dynamic ice sheet. Melt estimates for static, present-day cavity geometries should therefore be treated with caution. Moreover, geometrically-induced trends in

melt rates should be considered alongside anthropogenic climate trends, as they could greatly amplify or reduce the impact of climate change on the ice-shelf mass balance.

While it is well known that rates of grounded ice loss are regulated by the amount of buttressing provided by the adjacent ice shelves, results from this study suggest that melt-geometry feedbacks can play an important role in ~~offsetting shifts~~ controlling the dynamical connection between grounded and floating ice. For all glaciers except Kohler West Glacier, a sustained increase in grounding line discharge ~~, and thereby enable a sustained negative~~ by up to 30% is simulated, while changes in calving flux and total ice-shelf area are relatively small. Yet, the net mass balance of the ice shelves ~~, which drives further~~ remains negative. In all cases, the increased discharge across the grounding line is offset by a geometrically-induced increase in average basal melting, allowing further ice-shelf thinning, grounding line retreat and ~~ice-sheet~~ mass loss. While the glacier mechanics of this process have been well understood in principle, results in this study have highlighted the important role of ocean dynamics in controlling basal melt rates.

Code and data availability. The coupled-ice ocean model Úa-MITgcm is publicly available on GitHub (https://github.com/knaughten/UaMITgcm/), as are the stand-alone components of the ocean circulation model MITgcm (https://github.com/MITgcm/MITgcm/) and the ice dynamics model Úa (https://github.com/GHilmarG/UaSource/). The configuration files specific to the setup in this paper can be accessed via https://github.com/knaughten/UaMITgcm/tree/archer2/example/PTDC_999. All scripts that were used to process the raw MITgcm output and to produce the figures will be made publicly available on GitHub (https://github.com/janderydt) upon acceptance of the manuscript.

Appendix A: Model initialization and validation

The Úa-MITgcm simulations presented in the main part of the paper were preceded by a spin-up and hindcast simulation, ~~represented~~ as indicated by the flow diagram in Figure A1. Given the abundant evidence that ice-sheet models, either in standalone mode (Seroussi et al., 2019) or coupled to an ocean model (Goldberg and Holland, 2022), retain information about their initial state that can dominate the future evolution of the ice sheet, and the fact that diverse approaches to (coupled) model initialization are used in the literature, a detailed account of the Úa, MITgcm and Úa-MITgcm initialization procedures are provided in Sect. A1. A basic validation of the coupled configuration, based on a 1997-2014 hindcast simulation, is provided in Sect. A2.

A1 Initialization and spinup

As a first step in the initialization of the coupled Úa-MITgcm configuration, the ice flow model Úa was calibrated using an inverse method, first introduced by Macayeal (1992) and now frequently used in ice-sheet modelling (e.g. De Rydt et al. (2021); Barnes et al. (2021)). The inverse step resulted in optimal estimates of the spatially varying rate factor (A) in Glen's law and the slipperiness (C) in the basal sliding law, for a given ice-sheet geometry and surface velocity measurements (u_{obs}) with corresponding errors (ε_u). Values for the A and C fields were obtained as a solution to the minimization problem $\mathrm{d}_{[A,C]}J = 0$,
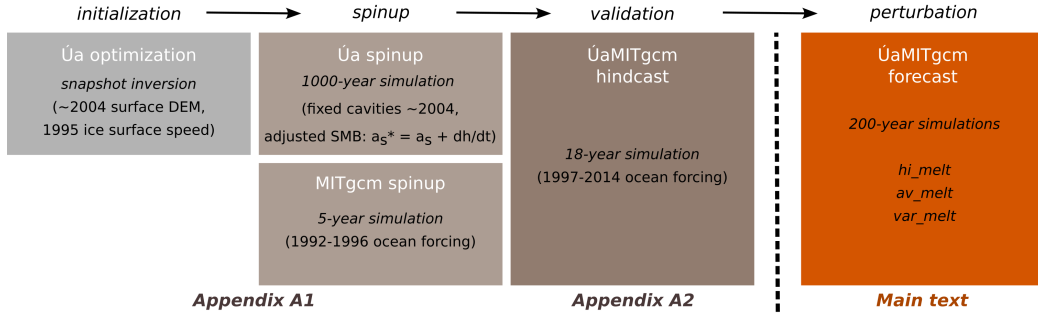
Figure A1. Flowchart showing the different steps in the intialization, spinup and validation of the coupled ice-ocean model Úa-MITgcm. Details about the initialization and spinup of the standalone Úa and MITgcm configurations are provided in Sect. A1. Results from a Úa-MITgcm hindcast simulation between 1997 and 2014 are provided in Sect. A1. Results from the 200-year perturbation experiments (*hi_melt*, *av_melt* and *var_melt*) are presented and discussed in the main part of the text.

where the cost function J was defined as the sum of the misfit terms for the surface velocities and ice thickness changes, and a Tikhonov regularization term: $J = I + R$, with

$$I = \frac{1}{2\mathcal{A}} \int d\mathbf{x} \left((u_{\mathrm{model}} - u_{\mathrm{obs}})^2 / \varepsilon_u^2 + \left(\partial_t h|_{\mathrm{model}} - \partial_t h|_{\mathrm{obs}} \right)^2 / \varepsilon_{\partial_t h}^2 \right) \tag{A1}$$

$$R = \frac{1}{2\mathcal{A}} \int d\mathbf{x} \sum_i \left(\gamma_{i,s}^2 \left(\nabla \log_{10} (p_i/\hat{p}_i) \right)^2 + \gamma_{i,a}^2 \left(\log_{10} (p_i/\hat{p}_i) \right)^2 \right), \tag{A2}$$

where $\mathcal{A} = \int d\mathbf{x} I$ is the total area of the domain, p_i and $\hat{p}_i$ with $i \in [1,2]$ are shorthand notation for $p_1 = A$, $p_2 = C$ and their respective priors $\hat{p}_1 = 5 \times 10^{-9}$ yr^{-1}kPa^{-3}, $\hat{p}_2 = 0.0015$ m yr^{-1}kPa^{-3}. Values of the pre-multipliers $\gamma_{A,s} = \gamma_{C,s} = 10^5$ and $\gamma_{A,a} = 250$, $\gamma_{C,a} = 1$ were chosen based on a common L-curve approach (De Rydt et al., 2021). The velocity observations (u_{obs}) and corresponding errors (ε_u) in the first misfit term were taken from the ERS-1/2 InSAR tandem mission in late 1995 - early 1996 (Rignot et al., 2004). Ice thickness changes were set to zero everywhere ($\partial_t h|_{\mathrm{obs}} = 0$) with errors $\varepsilon_{\partial_t h} = 0.1$ and $\varepsilon_{\partial_t h} = \infty$ for grounded and floating ice, respectively. The ice-sheet geometry was assembled from a combination of Bedmachine Antarctica v2 data for the bed geometry (Morlighem et al., 2020), and the Icesat-corrected surface DEM from the ERS-1/2 mission with effective timestamp in 2004 (Bamber and Griggs, 2009). Nominal ice densities (917 kg m^{-3}) were corrected using a climatology of the firn density and thickness distribution from the RACMO2.3 dataset between 1979 and 2013 (van Wessem et al., 2018). The inversion for A and C was stopped after 1000 iterations with a mean and standard deviation of the misfit between modelled and observed surface speed of 12 m yr^{-1} and 61 m yr^{-1}, respectively.

Following the inversion step, the transient evolution of the ice-sheet can be contaminated by unrealistic short-wavelength (< 10 km), large-amplitude (> 10 m/yr) adjustments that dominate changes in ice thickness during the first few years of the simulation. These adjustments arise from a force imbalance due to inconsistent and uncertain input data, the simplified physical description of ice flow, and errors in the external forcing such as the surface and basal mass balance. Importantly, the initial transient modes can stimulate the growth of unrealistic dynamic behaviour, which can drive the solution away from the observed trends. For example, a localized, short-lived increase in ice thickness at the grounding line can cause an advance of

the ice sheet, and induce a positive feedback between slow-down and further advance, independent of the observed trends. To dampen the spurious changes in ice thickness, whilst preventing the geometry to drift away from its present-day configuration, a spinup of the ice sheet was carried out with Úa in standalone mode (Fig. A1), following a method similar to Arthern and Williams (2017). The ice velocity and thickness were evolved for 1500 years with two constraints: the ice thickness was fixed to its initial value for all nodes that were afloat at time 0, and the surface mass balance of the grounded ice was modified by an additional term, $as \rightarrow as - \partial_t h$, where $\partial_t h$ corresponds to the spatially variable, time-average rate of ice thickness change between 1997 and 2001 from satellite measurements (IMBIE Team, 2018). After 1500 years, the ice sheet reached an approximate steady state, with a mean change and standard deviation in grounded ice thickness and surface velocities of -12.7 ± 54 m and -13.5 ± 55 m yr^{-1} compared to the initial state. Importantly, the ice-shelf extent, and therefore the grounding line location, remained approximately unchanged during the spinup simulation, with only a small inland migration in isolated areas. Moreover, any simulation that is started from the spinup state with surface mass balance as, will reproduce initial changes in grounded ice thickness that correspond to the observed rates of change in the late 1990s ($\partial_t h$ above).

The ice-sheet geometry at the end of the Úa spinup was transferred to MITgcm, and used in a five-year, ocean-only, spinup with static ice shelf cavities. This allowed the ocean state to adjust from its uniformly stratified initial conditions to a dynamic state in equilibrium with the varying boundary conditions. The latter correspond to 1992-1996 monthly mean values of temperature, salinity and velocity from Kimura et al. (2017), linearly interpolated onto the open ocean boundaries of the regional MITgcm configuration (Fig. 1). Given typical flow speeds of 0.01 m s^{-1}, a five-year spin-up period was considered adequate for the 450 km by 250 km ocean domain with relatively small ice shelf cavities. At the end of the ocean spinup (31/12/1996), the coupling between Úa and MITgcm was switched on (Fig. A1), and the coupled configuration was stepped forward with monthly-mean ocean restoring conditions between 01/01/1997 and 31/12/2014, based on Kimura et al. (2017). Results from this hindcast experiment, referred to as *var_melt*, are presented in the next section.

A2   Model validation

The performance of Úa-MITgcm in its configuration specific to this study, is assessed by comparing model output to available Earth Observation and in situ ocean data between January 1997 and December 2014. Whilst model validation is a crucial step towards certifying the model's ability to accurately predict future changes in Antarctic ice volume, a comprehensive validation exercise is not attempted here. It is recognised that further optimization of the current configuration is required in order to eliminate some of the biases that could play a distinctive role in future ice loss projections.

A comparison between modelled and observed changes in ice-sheet surface elevation and surface velocities between 1997 and 2015 are presented in Fig. A2. Whilst Úa-MITgcm simulates widespread negative changes in ice thickness with a spatial pattern that matches the observations, its magnitude and accompanying upstream migration of the grounding line between 1997 and 2015 is significantly underestimated. In agreement with the slower-than-observed changes in ice thickness, changes in surface velocity are smaller than observed. For all ice shelves except Pine Island Ice Shelf, the simulated change in surface speed has the opposite sign compared to observations. Whilst the sign and magnitude of the observed changes is ultimately simulated at later times in the different Úa-MITgcm perturbation experiments (*hi_melt*, *av_melt* and *var_melt* in Sect. 2.2), the
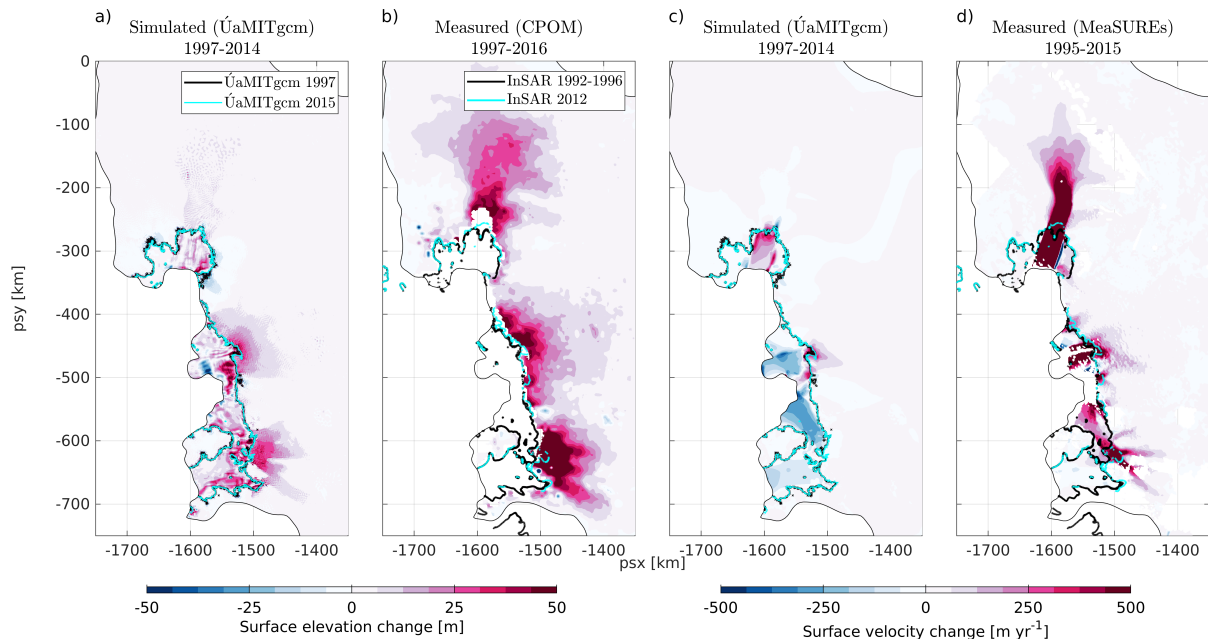
Figure A2. A comparison between simulated (a, c) and measured (b, d) changes in surface elevation change and surface velocity changes between 1997 and 2015. Simulated results are from the coupled Úa-MITgcm hindcast experiment *var_melt*, which starts from an initial ice-sheet geometry representative of the late 1990s - early 2000s, and is forced by ocean restoring conditions between 1997 and 2015 (Kimura et al., 2017). Observed changes in surface elevation of the grounded ice between 1997 and 2016 (panel b) were obtained from CPOM (IMBIE Team, 2018); changes in surface velocity (panel d) were provided by the MeaSUREs project (Rignot et al., 2017). Grounding line locations in 1997 and 2015 from Úa-MITgcm are shown in panels a and c in black and cyan, respectively. Corresponding estimates from InSAR data (panels b and d) were taken from Rignot et al. (2016).

ice-sheet response is delayed and depends strongly on the ocean forcing. The slower-than-observed response can be caused by a variety of poorly-constrained or missing processes, including but not limited to the form of the basal sliding law, the lack of ice-shelf damage evolution and calving front migration, and a potential misrepresentation of ocean-induced basal melting in shallow cavities with unknown bathymetry near the grounding line. A quantification of the uncertainties related to these

835   processes, and further optimization of the ice-ocean model will be pursued in future studies. In particular, the construction of an initial state that minimizes the misfit between simulated and observed trends in ice thickness and speed over the observational period is an essential requirement for the correct timing of any future mass loss from the West Antarctic Ice Sheet (Goldberg and Holland, 2022).

     A comparison between simulated and observed ice-shelf melt rates is provided in Fig. A3. Overall, integrated meltwater

840   fluxes from the coupled hindcast experiment (*var_melt*) agree well with observations, except for Pine Island Ice Shelf in 2012 and 2014, when the model overestimates basal mass loss by about 50%. The temporal variability of *var_melt* compares favorably to results from Naughten et al. (2022) (dashed blue line in Fig. A3), which include a more complete treatment
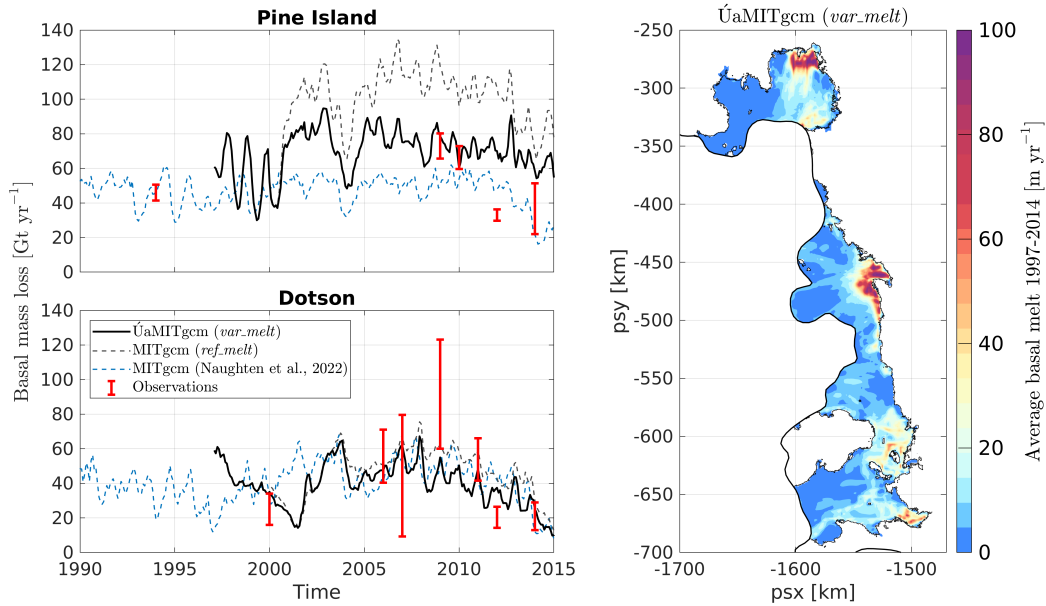
Figure A3. A comparison between simulated and measured net basal mass loss for the Pine Island and Dotson ice shelves. Results from the coupled Úa-MITgcm hindcast simulation (*var_melt*) and two stand-alone MITgcm simulations with fixed cavities (*ref_melt* and results from Naughten et al. (2022)) are compared to observations for the Pine Island Ice Shelf (years 1994, 2009, 2010 and 2012 from Dutrieux et al. (2014) and 2014 from Heywood et al. (2016)) and the Dotson Ice Shelf (Jenkins et al., 2018). The right panel shows average melt rates between 1997 and 2014 from the *var_melt* simulation.

of ocean-atmosphere interactions. The agreement is not surprising given the current setup uses restoring conditions at the ocean boundaries that were obtained from a regional ocean simulation by Kimura et al. (2017), which has a similar model

845 architecture as Naughten et al. (2022), and was forced by ERA-Interim atmospheric conditions that are similar to the improved ERA5 atmospheric conditions used in Naughten et al. (2022). The good agreement also holds true despite the absence of ocean surface fluxes in this study, which is an indication that the latter do not strongly affect the basal melt variability. Any remaining discrepancies between the current Úa-MITgcm configuration and Naughten et al. (2022), in particular for Pine Island Glacier, can be caused by a number of differences in ocean parameter choices, cavity geometry, boundary forcing, model resolution

850 etc., and a detailed comparison will not be pursued here. Results from a stand-alone MITgcm simulation with the same 1997-2014 ocean boundary restoring conditions but with fixed ice-shelf cavities (*ref_melt* experiment, dashed black line in Fig. A3), produced melt rates for Pine Island Ice Shelf about 50% higher than results from the corresponding *var_melt* experiment with evolving cavities. This highlights the important impact of changes in cavity geometry on basal melt rates, and the realization that the calibration of model parameters against observations can lead to distinctly different parameter choices for stand-alone

855 and coupled setups.

The spatial distribution of basal melt in the *var_melt* experiment, averaged between 1997 and 2014, is shown in Fig. A3. Average melt rates in excess of 100 m yr^{-1} are found near the grounding lines of Pine Island and Thwaites glaciers, while basal ablation of the Crosson and Dotson ice shelves is generally lower due to lower thermal driving of the far-field ocean (Sect. 4.2). While satellite observation-based estimates of basal melt rates are available for comparison (Gourmelen et al. (2017) and Adusumilli et al. (2018)), results are not reproduced here. Significant data gaps remain in regions with the highest melt rates near the grounding lines of Pine Island and Western Thwaites ice shelves, making it difficult to validate the simulated melt patterns in those regions.

Author contributions. JDR designed and initiated the project, performed the model simulations, carried out the analysis, and produced the figures and manuscript. KN coded the latest version of Úa-MITgcm and reviewed and edited the paper.

Competing interests. Jan De Rydt serves as topical editor for EGUSphere and The Cryosphere.

Acknowledgements. Jan De Rydt ~~was supported by~~ is supported by a UKRI Future Leaders Fellowship (MR/W011816/1) an by the TiPACCs project, which receives funding from the European Union's Horizon 2020 research and innovation programme under grant agreement no. 820575. Kaitlin Naughten is supported by the NERC LTSM project TerraFIRMA.

References

870 Adusumilli, S., Fricker, H. A., Medley, B., Padman, L., and Siegfried, M. R.: Interannual variations in meltwater input to the Southern Ocean from Antarctic ice shelves, Nature Geoscience, https://doi.org/10.1038/s41561-020-0616-z, http://dx.doi.org/10.1038/s41561-020-0616-z, 2018.

Arthern, R. J. and Williams, C. R.: The sensitivity of West Antarctica to the submarine melting feedback, Geophysical Research Letters, 44, 2352–2359, https://doi.org/10.1002/2017GL072514, 2017.

875 Bamber, J. L. and Griggs, J. A.: A new 1 km digital elevation model of the Antarctic derived from, The Cryosphere, 3, 101–111, http://www.the-cryosphere.net/3/101/2009/tc-3-101-2009.pdf, 2009.

Barnes, J. M., Dias Dos Santos, T., Goldberg, D., Hilmar Gudmundsson, G., Morlighem, M., and De Rydt, J.: The transferability of adjoint inversion products between different ice flow models, Cryosphere, 15, 1975–2000, https://doi.org/10.5194/tc-15-1975-2021, 2021.

Bradley, A. T., Bett, D. T., Dutrieux, P., De Rydt, J., and Holland, P. R.: The Influence of Pine Island Ice Shelf Calving on Basal Melting,
880 Journal of Geophysical Research: Oceans, 127, https://doi.org/10.1029/2022JC018621, 2022.

Cornford, S. L., Martin, D. F., Lee, V., Payne, A. J., and Ng, E. G.: Adaptive mesh refinement versus subgrid friction interpolation in simulations of Antarctic ice dynamics, Annals of Glaciology, 57, 1–9, https://doi.org/10.1017/aog.2016.13, 2016.

Davison, B. J., Hogg, A. E., Rigby, R., Veldhuijsen, S., van Wessem, J. M., van den Broeke, M. R., Holland, P. R., Selley, H. L., and Dutrieux, P.: Sea level rise from West Antarctic mass loss significantly modified by large snowfall anomalies, Nature Communications,
885 14, https://doi.org/10.1038/s41467-023-36990-3, 2023.

De Rydt, J., Holland, P. R., Dutrieux, P., and Jenkins, A.: Geometric and oceanographic controls on melting beneath Pine Island Glacier, Journal of Geophysical Research: Oceans, 119, 2420–2438, https://doi.org/10.1002/2013JC009513, 2014.

De Rydt, J., Reese, R., Paolo, F. S., and Hilmar Gudmundsson, G.: Drivers of Pine Island Glacier speed-up between 1996 and 2016, Cryosphere, 15, 113–132, https://doi.org/10.5194/tc-15-113-2021, 2021.

890 Depoorter, M. A., Bamber, J. L., Griggs, J. A., Lenaerts, J. T., Ligtenberg, S. R., Van Den Broeke, M. R., and Moholdt, G.: Calving fluxes and basal melt rates of Antarctic ice shelves, Nature, 502, 89–92, https://doi.org/10.1038/nature12567, 2013.

De Rydt, J. and Gudmundsson, G. H.: Coupled ice shelf-ocean modeling and complex grounding line retreat from a seabed ridge, Journal of Geophysical Research F: Earth Surface, 121, 865–880, https://doi.org/10.1002/2015JF003791, 2016.

Dutrieux, P., De Rydt, J., Jenkins, A., Holland, P. R., Ha, H. K., Lee, S. H., Steig, E. J., Ding, Q., Abrahamsen, E. P., and Schröder, M.:
895 Strong sensitivity of pine Island ice-shelf melting to climatic variability, Science, 343, 174–178, https://doi.org/10.1126/science.1244341, http://science.sciencemag.org/content/343/6167/174.abstract, 2014.

Edwards, T. L., Nowicki, S., Marzeion, B., Hock, R., Goelzer, H., Seroussi, H., Jourdain, N. C., Slater, D. A., Turner, F. E., Smith, C. J., McKenna, C. M., Simon, E., Abe-Ouchi, A., Gregory, J. M., Larour, E., Lipscomb, W. H., Payne, A. J., Shepherd, A., Agosta, C., Alexander, P., Albrecht, T., Anderson, B., Asay-Davis, X., Aschwanden, A., Barthel, A., Bliss, A., Calov, R., Chambers, C., Champollion,
900 N., Choi, Y., Cullather, R., Cuzzone, J., Dumas, C., Felikson, D., Fettweis, X., Fujita, K., Galton-Fenzi, B. K., Gladstone, R., Golledge, N. R., Greve, R., Hattermann, T., Hoffman, M. J., Humbert, A., Huss, M., Huybrechts, P., Immerzeel, W., Kleiner, T., Kraaijenbrink, P., Le clec'h, S., Lee, V., Leguy, G. R., Little, C. M., Lowry, D. P., Malles, J. H., Martin, D. F., Maussion, F., Morlighem, M., O'Neill, J. F., Nias, I., Pattyn, F., Pelle, T., Price, S. F., Quiquet, A., Radić, V., Reese, R., Rounce, D. R., Rückamp, M., Sakai, A., Shafer, C., Schlegel, N. J., Shannon, S., Smith, R. S., Straneo, F., Sun, S., Tarasov, L., Trusel, L. D., Van Breedam, J., van de Wal, R., van den Broeke, M.,

905   Winkelmann, R., Zekollari, H., Zhao, C., Zhang, T., and Zwinger, T.: Projected land ice contributions to twenty-first-century sea level rise, Nature, 593, 74–82, https://doi.org/10.1038/s41586-021-03302-y, 2021.

Goldberg, D. N. and Holland, P. R.: The Relative Impacts of Initialization and Climate Forcing in Coupled Ice Sheet-Ocean Modeling: Application to Pope, Smith, and Kohler Glaciers, Journal of Geophysical Research: Earth Surface, 127, https://doi.org/10.1029/2021JF006570, 2022.

910   Goldberg, D. N., Gourmelen, N., Kimura, S., Millan, R., and Snow, K.: How Accurately Should We Model Ice Shelf Melt Rates?, Geophysical Research Letters, 46, 189–199, https://doi.org/10.1029/2018GL080383, 2019.

Gourmelen, N., Goldberg, D. N., Snow, K., Henley, S. F., Bingham, R. G., Kimura, S., Hogg, A. E., Shepherd, A., Mouginot, J., Lenaerts, J. T., Ligtenberg, S. R., and van de Berg, W. J.: Channelized Melting Drives Thinning Under a Rapidly Melting Antarctic Ice Shelf, Geophysical Research Letters, 44, 9796–9804, https://doi.org/10.1002/2017GL074929, 2017.

915   Gudmundsson, G. H.: GHilmarG/UaSource: Ua2019b, https://doi.org/10.5281/zenodo.3706623, 2020.

Gudmundsson, G. H., Krug, J., Durand, G., Favier, L., and Gagliardini, O.: The stability of grounding lines on retrograde slopes, Cryosphere, 6, 1497–1505, https://doi.org/10.5194/tc-6-1497-2012, 2012.

Gudmundsson, G. H., Paolo, F. S., Adusumilli, S., and Fricker, H. A.: Instantaneous Antarctic ice sheet mass loss driven by thinning ice shelves, Geophysical Research Letters, 46, 13 903–13 909, https://doi.org/10.1029/2019GL085027, 2019.

920   Haseloff, M. and Sergienko, O. V.: The effect of buttressing on grounding line dynamics, Journal of Glaciology, 64, 417–431, https://doi.org/10.1017/jog.2018.30, 2018.

Heywood, K. J., Biddle, L. C., Boehme, L., Fedak, M., Dutrieux, P., Jenkins, A., Kaiser, J., Mallett, H., Jones, R. W., Naveira Garabato, A. C., Renfrew, I. A., Stevens, D. P., and Webber, B. G.: Between the devil and the deep blue sea: The role of the Amundsen Sea continental shelf in exchanges between ocean and ice shelves, Oceanography, 29, 118–129, https://doi.org/10.5670/oceanog.2016.104, 2016.

925   Holland, D. M. and Jenkins, A.: Modeling thermodynamic ice-ocean interactions at the base of an ice shelf, Journal of Physical Oceanography, 29, 1787–1800, https://doi.org/10.1175/1520-0485(1999)029<1787:mtioia>2.0.co;2, 1999.

Holland, P. R., Jenkins, A., and Holland, D. M.: The response of Ice shelf basal melting to variations in ocean temperature, Journal of Climate, 21, 2558–2572, https://doi.org/10.1175/2007JCLI1909.1, 2008.

Holland, P. R., O'connor, G. K., Bracegirdle, T. J., Dutrieux, P., Naughten, K. A., Steig, E. J., Schneider, D. P., Jenkins, A., and Smith,
930   J. A.: Anthropogenic and internal drivers of wind changes over the Amundsen Sea, West Antarctica, during the 20th and 21st centuries, Cryosphere, 16, 5085–5105, https://doi.org/10.5194/tc-16-5085-2022, 2022.

Holland, P. R., Bevan, S. L., and Luckman, A. J.: Strong Ocean Melting Feedback During the Recent Retreat of Thwaites Glacier, Geophysical Research Letters, 50, https://doi.org/10.1029/2023GL103088, 2023.

IMBIE Team: Mass balance of the Antarctic Ice Sheet from 1992 to 2017, Nature, 558, 219–222, https://doi.org/10.1038/s41586-018-0179-y,
935   http://www.nature.com/articles/s41586-018-0179-y, 2018.

Jacobs, S. S. and Hellmer, H. H.: Freshening Could Come From Other Melting Ice in the, Observatory, 23, 957–960, 1996.

Jenkins, A.: A one-dimensional model of ice shelf-ocean interaction, Journal of Geophysical Research, 96, 20 671, https://doi.org/10.1029/91jc01842, 1991.

Jenkins, A.: A simple model of the ice shelf-ocean boundary layer and current, Journal of Physical Oceanography, 46, 1785–1803,
940   https://doi.org/10.1175/JPO-D-15-0194.1, 2016.

Jenkins, A. and Bombosch, A.: Modeling the effects of frazil ice crystals on the dynamics and thermodynamics of Ice Shelf Water plumes, Journal of Geophysical Research, 100, 6967, https://doi.org/10.1029/94JC03227, 1995.

Jenkins, A., Nicholls, K. W., and Corr, H. F.: Observation and parameterization of ablation at the base of Ronne Ice Ahelf, Antarctica, Journal of Physical Oceanography, 40, 2298–2312, https://doi.org/10.1175/2010JPO4317.1, 2010.

945 Jenkins, A., Dutrieux, P., Jacobs, S., Steig, E. J., Gudmundsson, G. H., Smith, J., and Heywood, K. J.: Decadal Ocean Forcing and Antarctic Ice Sheet Response: LESSONS FROM THE AMUNDSEN SEA, 29, 106–117, https://doi.org/10.2307/24862286, https://www.jstor.org/stable/10.2307/24862286?seq=1&cid=pdf-, 2016.

Jenkins, A., Shoosmith, D., Dutrieux, P., Jacobs, S., Kim, T. W., Lee, S. H., Ha, H. K., and Stammerjohn, S.: West Antarctic Ice Sheet retreat in the Amundsen Sea driven by decadal oceanic variability, Nature Geoscience, 11, 733–738, https://doi.org/10.1038/s41561-018-0207-4, 950 http://dx.doi.org/10.1038/s41561-018-0207-4, 2018.

Joughin, I., Smith, B. E., and Schoof, C. G.: Regularized Coulomb Friction Laws for Ice Sheet Sliding: Application to Pine Island Glacier, Antarctica, Geophysical Research Letters, 46, 4764–4771, https://doi.org/10.1029/2019GL082526, 2019.

Joughin, I., Shapero, D., Smith, B., Dutrieux, P., and Barham, M.: Ice-shelf retreat drives recent Pine Island Glacier speedup, Science Advances, 7, 3080–3091, https://doi.org/10.1126/sciadv.abg3080, https://www.science.org/doi/10.1126/sciadv.abg3080, 2021.

955 Jourdain, N. C., Mathiot, P., Merino, N., Durand, G. G., Le Sommer, J., Spence, P., Dutrieux, P., Madec, G., Sommer, J. L., Spence, P., Dutrieux, P., and Madec, G.: Ocean circulation and sea-ice thinning induced by melting ice shelves in the Amundsen Sea, Journal of Geophysical Research: Oceans, 122, 2550–2573, https://doi.org/10.1002/2016JC012509, http://doi.wiley.com/10.1002/2016JC012509, 2017.

Jourdain, N. C., Mathiot, P., Burgard, C., Caillet, J., and Kittel, C.: Ice Shelf Basal Melt Rates in the Amundsen Sea at the End of the 21st 960 Century, Geophysical Research Letters, 49, https://doi.org/10.1029/2022GL100629, 2022a.

Jourdain, N. C., Mathiot, P., Burgard, C., Caillet, J., and Kittel, C.: Ice shelf basal melt rates in the Amundsen Sea at the end of the 21st cen-tury, Geophysical Research Letters, https://doi.org/10.1029/2022GL100629, https://onlinelibrary.wiley.com/doi/10.1029/2022GL100629, 2022b.

Kimura, S., Jenkins, A., Regan, H., Holland, P. R., Assmann, K. M., Whitt, D. B., Van Wessem, M., van de Berg, W. J., Reijmer, C. H., and 965 Dutrieux, P.: Oceanographic Controls on the Variability of Ice-Shelf Basal Melting and Circulation of Glacial Meltwater in the Amundsen Sea Embayment, Antarctica, Journal of Geophysical Research: Oceans, 122, 10 131–10 155, https://doi.org/10.1002/2017JC012926, 2017.

Lazeroms, W. M., Jenkins, A., Rienstra, S. W., and Van De Wal, R. S.: An analytical derivation of ice-shelf basal melt based on the dynamics of meltwater plumes, Journal of Physical Oceanography, 49, 917–939, https://doi.org/10.1175/JPO-D-18-0131.1, 2019.

Lhermitte, S., Sun, S., Shuman, C., Wouters, B., Pattyn, F., Wuite, J., Berthier, E., and Nagler, T.: Damage accelerates ice shelf in-970 stability and mass loss in Amundsen Sea Embayment, Proceedings of the National Academy of Sciences, 117, 24 735–24 741, https://doi.org/10.1073/pnas.1912890117, https://pnas.org/doi/full/10.1073/pnas.1912890117, 2020.

Losch, M.: Modeling ice shelf cavities in a z coordinate ocean general circulation model, Journal of Geophysical Research: Oceans, 113, https://doi.org/10.1029/2007JC004368, 2008.

Macayeal, D. R.: The basal stress distribution of ice stream E, Antarctica, inferred by control methods, Journal of Geophysical Research, 97, 975 595–603, https://doi.org/10.1029/91JB02454, 1992.

Marshall, J., Hill, C., Perelman, L., and Adcroft, A.: NON-HYDRQ, 102, 5733–5752, 1997.

Milillo, P., Rignot, E., Rizzoli, P., Scheuchl, B., Mouginot, J., Bueso-Bello, J., and Prats-Iraola, P.: Heterogeneous retreat and ice melt of thwaites glacier, West Antarctica, Science Advances, 5, 1–9, https://doi.org/10.1126/sciadv.aau3433, 2019.

Milillo, P., Rignot, E., Rizzoli, P., Scheuchl, B., Mouginot, J., Bueso-Bello, J. L., Prats-Iraola, P., and Dini, L.: Rapid glacier retreat rates 980 observed in West Antarctica, Nature Geoscience, 15, 48–53, https://doi.org/10.1038/s41561-021-00877-z, 2022.

Morlighem, M., Rignot, E., Binder, T., Blankenship, D., Drews, R., Eagles, G., Eisen, O., Ferraccioli, F., Forsberg, R., Fretwell, P., Goel, V., Greenbaum, J. S., Gudmundsson, H., Guo, J., Helm, V., Hofstede, C., Howat, I., Humbert, A., Jokat, W., Karlsson, N. B., Lee, W. S., Matsuoka, K., Millan, R., Mouginot, J., Paden, J., Pattyn, F., Roberts, J., Rosier, S., Ruppel, A., Seroussi, H., Smith, E. C., Steinhage, D., Sun, B., Broeke, M. R. d., Ommen, T. D., Wessem, M. v., and Young, D. A.: Deep glacial troughs and stabilizing ridges unveiled beneath the margins of the Antarctic ice sheet, Nature Geoscience, 13, 132–137, https://doi.org/10.1038/s41561-019-0510-8, http://dx.doi.org/10.1038/s41561-019-0510-8, 2020.

Mouginot, J., Rignot, E., and Scheuchl, B.: Sustained increase in ice discharge from the Amundsen Sea Embayment, West Antarctica, from 1973 to 2013, Geophysical Research Letters, 41, 1576–1584, https://doi.org/10.1002/2013GL059069, 2014.

Naughten, K. A. and De Rydt, J.: Ua-MITgcm PTDC configuration (Version 1.2), https://doi.org/10.5281/zenodo.7989869, 2023.

Naughten, K. A., Meissner, K. J., Galton-Fenzi, B. K., England, M. H., Timmermann, R., and Hellmer, H. H.: Future Projections of Antarctic Ice Shelf Melting Based on CMIP5 Scenarios, https://doi.org/10.1175/JCLI-D-17-0854.s1, https://doi.org/10.1175/JCLI-D-17-0854.s1., 2018.

Naughten, K. A., De Rydt, J., Rosier, S. H., Jenkins, A., Holland, P. R., and Ridley, J. K.: Two-timescale response of a large Antarctic ice shelf to climate change, Nature Communications, 12, https://doi.org/10.1038/s41467-021-22259-0, 2021.

Naughten, K. A., Holland, P. R., Dutrieux, P., Kimura, S., Bett, D. T., and Jenkins, A.: Simulated Twentieth-Century Ocean Warming in the Amundsen Sea, West Antarctica, Geophysical Research Letters, 49, https://doi.org/10.1029/2021GL094566, 2022.

Naughten, K. A., Holland, P. R., and De Rydt, J.: Unavoidable future increase in West Antarctic ice-shelf melting over the twenty-first century, Nature Climate Change, 13, 1222–1228, https://doi.org/10.1038/s41558-023-01818-x, 2023.

Otosaka, I. N., Shepherd, A., Ivins, E. R., Schlegel, N.-J., Amory, C., van den Broeke, M. R., Horwath, M., Joughin, I., King, M. D., Krinner, G., Nowicki, S., Payne, A. J., Rignot, E., Scambos, T., Simon, K. M., Smith, B. E., Sørensen, L. S., Velicogna, I., Whitehouse, P. L., A, G., Agosta, C., Ahlstrøm, A. P., Blazquez, A., Colgan, W., Engdahl, M. E., Fettweis, X., Forsberg, R., Gallée, H., Gardner, A., Gilbert, L., Gourmelen, N., Groh, A., Gunter, B. C., Harig, C., Helm, V., Khan, S. A., Kittel, C., Konrad, H., Langen, P. L., Lecavalier, B. S., Liang, C.-C., Loomis, B. D., McMillan, M., Melini, D., Mernild, S. H., Mottram, R., Mouginot, J., Nilsson, J., Noël, B., Pattle, M. E., Peltier, W. R., Pie, N., Roca, M., Sasgen, I., Save, H. V., Seo, K.-W., Scheuchl, B., Schrama, E. J. O., Schröder, L., Simonsen, S. B., Slater, T., Spada, G., Sutterley, T. C., Vishwakarma, B. D., van Wessem, J. M., Wiese, D., van der Wal, W., and Wouters, B.: Mass balance of the Greenland and Antarctic ice sheets from 1992 to 2020, Earth System Science Data, 15, 1597–1616, https://doi.org/10.5194/essd-15-1597-2023, https://essd.copernicus.org/articles/15/1597/2023/, 2023.

Paolo, F. S., Fricker, H. A., and Padman, L.: Volume loss from Antarctic ice shelves is accelerating, Science, 348, 327–331, https://doi.org/10.1126/science.aaa0940, 2015.

Paolo, F. S., Gardner, A. S., Greene, C. A., Nilsson, J., Schodlok, M. P., Schlegel, N. J., and Fricker, H. A.: Widespread slowdown in thinning rates of West Antarctic ice shelves, Cryosphere, 17, 3409–3433, https://doi.org/10.5194/tc-17-3409-2023, 2023.

Patmore, R. D., Holland, P. R., Munday, D. R., Naveira Garabato, A. C., Stevens, D. P., Meredith, M. P., Patmore, R. D., Holland, P. R., Munday, D. R., Garabato, A. C. N., Stevens, D. P., and Meredith, M. P.: Topographic Control of Southern Ocean Gyres and the Antarctic Circumpolar Current: A Barotropic Perspective, Journal of Physical Oceanography, pp. 19–0083, https://doi.org/10.1175/JPO-D-19-0083.1, http://journals.ametsoc.org/doi/10.1175/JPO-D-19-0083.1, 2019.

Pattyn, F., Schoof, C., Perichon, L., Hindmarsh, R. C., Bueler, E., De Fleurian, B., Durand, G., Gagliardini, O., Gladstone, R., Goldberg, D., Gudmundsson, G. H., Huybrechts, P., Lee, V., Nick, F. M., Payne, A. J., Pollard, D., Rybak, O., Saito, F., and Vieli, A.: Results of the marine ice sheet model intercomparison project (MISMIP+), Cryosphere, 6, 573–588, https://doi.org/10.5194/tc-6-573-2012, 2012.

Pedersen, F. B.: Dense bottom currents in rotating ocean, J. Hydraul. Div. Am. Soc. Civ. Eng., 106, 1291–1308, 1980.

1020 Pegler, S. S.: Marine ice sheet dynamics: The impacts of ice-shelf buttressing, Journal of Fluid Mechanics, 857, 605–647, https://doi.org/10.1017/jfm.2018.741, 2018.

Pritchard, H. D., Ligtenberg, S. R., Fricker, H. A., Vaughan, D. G., Van Den Broeke, M. R., and Padman, L.: Antarctic ice-sheet loss driven by basal melting of ice shelves, Nature, 484, 502–505, https://doi.org/10.1038/nature10968, 2012.

Reese, R., Garbe, J., Hill, E. A., Urruty, B., Naughten, K. A., Gagliardini, O., Durand, G., Gillet-Chaulet, F., Chandler, D., Langebroek,
1025 P. M., and Winkelmann, R.: The stability of present-day Antarctic grounding lines-Part B: Possible commitment of regional collapse under current climate, The Cryosphere, https://doi.org/10.5194/tc-2022-105, https://doi.org/10.5194/tc-2022-105, 2023.

Rignot, E., Thomas, R. H., Kanagaratnam, P., Casassa, G., Frederick, E., Gogineni, S., Krabill, W., Rivera, A., Russell, R., Sonntag, J., Swift, R., and Yungel, J.: Improved estimation of the mass balance of glaciers draining into the Amundsen Sea sector of West Antarctica from the CECS/NASA 2002 campaign, Annals of Glaciology, 39, 231–237, https://doi.org/10.3189/172756404781813916, 2004.

1030 Rignot, E., Mouginot, J., and Scheuchl, B.: MEaSUREs Antarctic Grounding Line from Differential Satellite Radar Interferometry, Version 2, 2016.

Rignot, E., Mouginot, J., and Scheuchl, B.: MEaSUREs InSAR-Based Antarctica Ice Velocity Map, Version 2, Boulder, Colorado USA. NASA National Snow and Ice Data Center Distributed Active Archive Center, 2017.

Rignot, E., Mouginot, J., Scheuchl, B., Van Den Broeke, M., Van Wessem, M. J., and Morlighem, M.: Four decades of Antarctic ice sheet
1035 mass balance from 1979–2017, Proceedings of the National Academy of Sciences of the United States of America, 116, 1095–1103, https://doi.org/10.1073/pnas.1812883116, 2019.

Seroussi, H. and Morlighem, M.: Representation of basal melting at the grounding line in ice flow models, Cryosphere, 12, 3085–3096, https://doi.org/10.5194/tc-12-3085-2018, 2018.

Seroussi, H., Nowicki, S., Simon, E., Abe-Ouchi, A., Albrecht, T., Brondex, J., Cornford, S., Dumas, C., Gillet-Chaulet, F., Goelzer, H.,
1040 Golledge, N. R., Gregory, J. M., Greve, R., Hoffman, M. J., Humbert, A., Huybrechts, P., Kleiner, T., Larour, E., Leguy, G., Lipscomb, W. H., Lowry, D., Mengel, M., Morlighem, M., Pattyn, F., Payne, A. J., Pollard, D., Price, S. F., Quiquet, A., Reerink, T. J., Reese, R., Rodehacke, C. B., Schlegel, N. J., Shepherd, A., Sun, S., Sutter, J., Van Breedam, J., Van De Wal, R. S., Winkelmann, R., and Zhang, T.: InitMIP-Antarctica: An ice sheet model initialization experiment of ISMIP6, Cryosphere, 13, 1441–1471, https://doi.org/10.5194/tc-13-1441-2019, 2019.

1045 Seroussi, H., Nowicki, S., Payne, A. J., Goelzer, H., Lipscomb, W. H., Abe-Ouchi, A., Agosta, C., Albrecht, T., Asay-Davis, X., Barthel, A., Calov, R., Cullather, R., Dumas, C., Galton-Fenzi, B. K., Gladstone, R., Golledge, N. R., Gregory, J. M., Greve, R., Hattermann, T., Hoffman, M. J., Humbert, A., Huybrechts, P., Jourdain, N. C., Kleiner, T., Larour, E., Leguy, G. R., Lowry, D. P., Little, C. M., Morlighem, M., Pattyn, F., Pelle, T., Price, S. F., Quiquet, A., Reese, R., Schlegel, N. J., Shepherd, A., Simon, E., Smith, R. S., Straneo, F., Sun, S., Trusel, L. D., Breedam, J. V., Van De Wal, R. S., Winkelmann, R., Zhao, C., Zhang, T., and Zwinger, T.: ISMIP6 Antarctica: A multi-model
1050 ensemble of the Antarctic ice sheet evolution over the 21st century, Cryosphere, 14, 3033–3070, https://doi.org/10.5194/tc-14-3033-2020, 2020.

Shepherd, A., Gilbert, L., Muir, A. S., Konrad, H., McMillan, M., Slater, T., Briggs, K. H., Sundal, A. V., Hogg, A. E., and Engdahl, M. E.: Trends in Antarctic Ice Sheet Elevation and Mass, Geophysical Research Letters, 46, 8174–8183, https://doi.org/10.1029/2019GL082182, 2019.

1055 Siahaan, A., Smith, R. S., Holland, P. R., Jenkins, A., Gregory, J. M., Lee, V., Mathiot, P., Payne, A. J., Ridley, J. K., and Jones, C. G.: The Antarctic contribution to 21st-century sea-level rise predicted by the UK Earth System Model with an interactive ice sheet, Cryosphere, 16, 4053–4086, https://doi.org/10.5194/tc-16-4053-2022, 2022.

Silvano, A., Holland, P. R., Naughten, K. A., Dragomir, O., Dutrieux, P., Jenkins, A., Si, Y., Stewart, A. L., Peña Molino, B., Janzing, G. W., Dotto, T. S., and Naveira Garabato, A. C.: Baroclinic Ocean Response to Climate Forcing Regulates Decadal Variability of Ice-Shelf
1060 Melting in the Amundsen Sea, Geophysical Research Letters, 49, https://doi.org/10.1029/2022GL100646, 2022.

Smith, B., Fricker, H. A., Gardner, A. S., Medley, B., Nilsson, J., Paolo, F. S., Holschuh, N., Adusumilli, S., Brunt, K., Csatho, B., Harbeck, K., Markus, T., Neumann, T., Siegfried, M. R., and Zwally, H. J.: Pervasive ice sheet mass loss reflects competing ocean and atmosphere processes, Science, 368, 1239–1242, https://doi.org/10.1126/science.aaz5845, https://www.science.org/doi/10.1126/science.aaz5845, 2020.

1065 Smith, J. A., Andersen, T. J., Shortt, M., Gaffney, A. M., Truffer, M., Stanton, T. P., Bindschadler, R., Dutrieux, P., Jenkins, A., Hillenbrand, C. D., Ehrmann, W., Corr, H. F., Farley, N., Crowhurst, S., and Vaughan, D. G.: Sub-ice-shelf sediments record history of twentieth-century retreat of Pine Island Glacier, Nature, 541, 77–80, https://doi.org/10.1038/nature20136, 2017.

Surawy-Stepney, T., Hogg, A. E., Cornford, S. L., and Davison, B. J.: Episodic dynamic change linked to damage on the thwaites glacier ice tongue, Nature Geoscience, https://doi.org/10.1038/s41561-022-01097-9, 2023.

1070 Timmermann, R. and Hellmer, H. H.: Southern Ocean warming and increased ice shelf basal melting in the twenty-first and twenty-second centuries based on coupled ice-ocean finite-element modelling, Ocean Dynamics, 63, 1011–1026, https://doi.org/10.1007/s10236-013-0642-0, 2013.

van Wessem, J. M., van de Berg, W. J., Noël, B. P. Y., van Meijgaard, E., Amory, C., Birnbaum, G., Jakobs, C. L., Krüger, K., Lenaerts, J. T. M., Lhermitte, S., Ligtenberg, S. R. M., Medley, B., Reijmer, C. H., van Tricht, K., Trusel, L. D., van Ulft, L. H., Wouters, B., Wuite,
1075 J., and van den Broeke, M. R.: Modelling the climate and surface mass balance of polar ice sheets using RACMO2 – Part 2: Antarctica (1979–2016), The Cryosphere, 12, 1479–1498, https://doi.org/10.5194/tc-12-1479-2018, https://tc.copernicus.org/articles/12/1479/2018/, 2018.

Weertman, J.: Stability of the Junction of an Ice Sheet and an Ice Shelf, Journal of Glaciology, 13, 3–11, https://doi.org/10.3189/s0022143000023327, 1974.

1080 Zhao, K. X., Stewart, A. L., and McWilliams, J. C.: Sill-Influenced Exchange Flows in Ice Shelf Cavities, Journal of Physical Oceanography, 49, 163–191, https://doi.org/10.1175/JPO-D-18-0076.1, https://journals.ametsoc.org/view/journals/phoc/49/1/jpo-d-18-0076.1.xml, 2019.